



# Molecular Dynamics Studies of Grain Boundary Mobility and Anisotropy in BCC $\alpha$ - Uranium

July 2022

*Changing the World's Energy Future*

Jarin French, Xian-Ming Bai



**DISCLAIMER**

This information was prepared as an account of work sponsored by an agency of the U.S. Government. Neither the U.S. Government nor any agency thereof, nor any of their employees, makes any warranty, expressed or implied, or assumes any legal liability or responsibility for the accuracy, completeness, or usefulness, of any information, apparatus, product, or process disclosed, or represents that its use would not infringe privately owned rights. References herein to any specific commercial product, process, or service by trade name, trade mark, manufacturer, or otherwise, does not necessarily constitute or imply its endorsement, recommendation, or favoring by the U.S. Government or any agency thereof. The views and opinions of authors expressed herein do not necessarily state or reflect those of the U.S. Government or any agency thereof.

# **Molecular Dynamics Studies of Grain Boundary Mobility and Anisotropy in BCC $\alpha$ -Uranium**

**Jarin French, Xian-Ming Bai**

**July 2022**

**Idaho National Laboratory  
Idaho Falls, Idaho 83415**

**<http://www.inl.gov>**

**Prepared for the  
U.S. Department of Energy  
Under DOE Idaho Operations Office  
Contract DE-AC07-05ID14517**

# Molecular Dynamics Studies of Grain Boundary Mobility and Anisotropy in BCC $\gamma$ -Uranium

Jarin French<sup>1</sup>, Xian-Ming Bai<sup>1,2\*</sup>

<sup>1</sup>Department of Materials Science and Engineering, Virginia Polytechnic Institute and State University, Blacksburg, VA 24061, USA

<sup>2</sup>Computational Mechanics and Materials Department, Idaho National Laboratory, Idaho Falls, ID 83415, USA

## Abstract

Grain morphologies such as grain size and aspect ratio in uranium-based metallic fuels are important microstructural features that can impact various fuel performance properties such as fission-gas-induced swelling, thermal transport, high burnup structure formation, and radiation resistance. Accurate prediction of the fuel grain morphologies requires knowledge of critical grain growth parameters such as grain boundary (GB) mobility and anisotropy. In this work, molecular dynamics (MD) simulations were performed to study the GB mobility of and its anisotropy in pure body-centered-cubic (BCC)  $\gamma$  uranium. Nine GBs with different combinations of misorientation angles ( $20^\circ$ ,  $30^\circ$ ,  $45^\circ$ ) and rotation axes ( $\langle 100 \rangle$ ,  $\langle 110 \rangle$ ,  $\langle 111 \rangle$ ), as well as an additional  $\langle 111 \rangle$   $38.2^\circ$  GB were studied using three interatomic potentials. It is found that the GB mobility anisotropy has complex trends, depending on both rotation axis and misorientation. However, in general the  $\langle 110 \rangle$  rotation axis has the fastest GB mobility at the same misorientation. The results of this work can be used as not only a baseline for future studies of GB mobility in uranium-based alloys such as uranium-molybdenum (U-Mo) fuels, but also as input for mesoscale modeling of grain growth in uranium-based alloys.

Keywords: uranium based metallic fuels; grain boundary mobility and anisotropy; grain growth; molecular dynamics simulation

\*Corresponding author.

Email address: [xmbai@vt.edu](mailto:xmbai@vt.edu) (X.M. Bai)

## 1. Introduction

The Global Threat Reduction Initiative (GTRI) Convert program has driven scientific understanding of nuclear fuels with high uranium (U) density and low enrichment through subprograms such as the US High Performance Research Reactor (USHPRR) conversion program.<sup>1,2</sup> Pure U has a high density, making it a good candidate fuel form for this purpose. However, the stable phase of pure U is the  $\alpha$  phase at temperatures below 668 °C, which has an orthorhombic crystal structure and thus unsatisfactory radiation performance.<sup>3-5</sup> When the temperatures are above the temperature range for stable  $\alpha$  phase, the first stable crystal structure is a complex tetragonal  $\beta$  structure.<sup>6</sup> At temperatures above 776 °C (1049 K), pure U has a body-centered-cubic (BCC)  $\gamma$  phase with good radiation tolerance.<sup>5</sup> Unfortunately, this temperature range is much higher than the typical operation temperatures of research and test reactors, which are usually lower than 250 °C.<sup>5,7</sup> It has been found that alloying U with molybdenum (Mo) can stabilize the desired BCC  $\gamma$  phase in the research reactor temperature range,<sup>5</sup> even though the stabilized  $\gamma$  phase is metastable according to the U-Mo phase diagram.<sup>8,9</sup> Therefore, the U-Mo based metallic fuel system has been particularly focused on for its very high U density<sup>10</sup> and satisfactory fuel performance properties, such as high thermal conductivity,<sup>11,12</sup> good fission gas stability,<sup>5,13</sup> and excellent radiation resistance.<sup>5,14</sup> In terms of fuel design, both monolithic and dispersion U-Mo fuel forms have been extensively studied.<sup>8</sup> The typical fuel compositions are U-10wt.%Mo and U-7wt.%Mo, which are commonly referred as U-10Mo and U-7Mo in literature.<sup>5</sup>

However, one glaring weakness of U-Mo fuels is the accelerated fuel swelling observed at high fission density or burnup.<sup>15-17</sup> At low fission densities, U-Mo fuel swelling increases almost linearly with fission density, which is mainly induced by solid fission products.<sup>16-18</sup> At these lower fission densities, fission gases such as xenon (Xe) and krypton (Kr) can precipitate and form a stable face-centered-cubic (FCC) nano-bubble superlattice in the BCC U-Mo so that the gas bubble swelling effect is suppressed.<sup>18,19</sup> At a threshold fission density, the fuel swelling deviates from the linear behavior and increases rapidly.<sup>15,16,18</sup> Such an accelerated fuel swelling behavior is closely related to the formation of large intergranular fission gas bubbles.<sup>18</sup> It has been found that the onset of the accelerated fuel swelling coincides with the high burnup structure (HBS) formation.<sup>16,18</sup> The HBS formation is a grain subdivision process (i.e., a large grain splits into many small grains), which has been observed in both U-Mo-based metallic fuels<sup>8,18,20</sup> and uranium dioxide (UO<sub>2</sub>)-based oxide fuels<sup>21</sup> at high burnups. The small grain size in the HBS can reduce the diffusion length of fission gas atoms from grain interior to grain boundaries (GBs). In addition, the high-density GBs in the HBS can provide fast diffusion paths for insoluble fission gas atoms to precipitate into large intergranular bubbles. Previous phase field modeling<sup>22,23</sup> and experimental studies<sup>15,17,20</sup> have identified that the initial grain morphology plays a vital role in affecting the onset of HBS formation and the accompanying accelerated fuel swelling. Typically, an increased average grain size and reduced grain aspect ratio delay the HBS formation and thus fuel swelling.<sup>14,22,24-26</sup> This is because GBs are favorable nucleation sites for HBS formation. If the initial average grain size is large, the number of HBS nucleation sites is low and therefore the HBS formation occurs at high fission densities. Thus, an ideal fuel microstructure for delaying the accelerated fuel swelling would consist of large and equiaxed grains.<sup>27</sup> Since the swelling behavior of U-Mo fuels must be stable and predictable to meet safety requirements, the knowledge of how the fuel microstructure changes is important in determining the processing parameters used to create the fuel, as well as the operating parameters for the desired fuel performance. This

knowledge can also be applied to fuel performance modeling codes (e.g., MARMOT<sup>28</sup>) to predict the microstructural evolution during fuel fabrication as well as in the reactors relevant conditions.

Since the initial fuel microstructure (more specifically, grain size and aspect ratio) is very important for the long-term U-Mo fuel performance in reactors, the initial fuel grain morphology needs to be controlled within specific parameters. During fuel fabrication, high-temperature treatment is usually used to control the grain growth. Many experiments have shown that  $\gamma$  phase U-Mo alloys can have significant grain growth at high temperatures.<sup>27,29–31</sup> From the time ( $t$ ) evolution of the average grain size ( $D$ ), a grain growth constant ( $K$ ) can be extracted based on the ideal grain growth model

$$D^2 - D_0^2 = Kt, \quad (1)$$

where  $D_0$  is the initial grain size.<sup>27,32</sup> The grain growth constant is closely related to GB mobility.<sup>33</sup> The underlying assumption of such an analysis is that the GB mobility is isotropic, i.e., does not depend on the GB character. Some researchers also used mesoscale phase field modeling to predict the grain growth of U-Mo fuels under high-temperature treatment.<sup>23,34</sup> The GB-mobility-related kinetic parameters were empirically fitted from experimental data and thus are isotropic as well. Although such an approximation can lead to satisfactory prediction of grain growth at specific fuel fabrication conditions, the effect of anisotropy in GB properties is largely ignored. Grain growth is determined in part by two GB properties: GB energy and mobility, both of which are anisotropic.<sup>35,36</sup> Previously, researchers have used density functional theory (DFT)<sup>23</sup> or molecular dynamics (MD)<sup>37</sup> to calculate GB energies in U-Mo fuels. Although the results show that GB energy is anisotropic, it only varies less than 75% for the studied GBs.<sup>23,37</sup> For GB mobility in U or U-based alloys, to the best of the authors' knowledge there are no experimental data or theoretical studies to directly demonstrate its anisotropic behavior. However, the average GB mobilities extracted from various U-Mo grain growth experiments are scattered, e.g., sometimes it can vary by a factor of 10 at the same temperature.<sup>11,23,30,31</sup> In addition, in other materials such as aluminum (Al) the GB mobility can vary by a few orders of magnitude, depending on the GB character.<sup>38,39</sup> Therefore, it is reasonably expected that GB mobilities in U-based metals are also anisotropic, although such information is still lacking to date. The effect of GB mobility anisotropy on grain growth morphology is controversial as some computational studies show that the mobility anisotropy alone has little effect on the final grain texture,<sup>40–43</sup> while others give contradictory conclusions.<sup>44</sup> However, some of these studies also show that the combination of both GB energy anisotropy and mobility anisotropy can have significant impact on the grain growth kinetics, local microstructures, and overall grain morphologies.<sup>42,45</sup> Therefore, if more sophisticated grain growth models are needed for more accurate fuel performance modeling, an in-depth understanding of the GB mobility anisotropy is a requirement.

GBs have five macroscopic degrees of freedom,<sup>39</sup> creating a large parameter space to determine the anisotropic GB properties. Performing extensive experiments to map GB energies and mobilities in this five-parameter space is therefore impractical. Currently, most reported anisotropic GB properties are for GB energies.<sup>46,47</sup> Within the limited reports of anisotropic GB mobilities, most of them focus on FCC metals such as Al and nickel (Ni).<sup>39,48</sup> For Al, it has been found that both rotation axis and misorientation angle can have significant effects on GB mobility. In general, the  $\langle 111 \rangle$  rotation axis gives the fastest GB mobility compared to other low-index rotation axes (e.g.,  $\langle 100 \rangle$  and  $\langle 110 \rangle$ ).<sup>39,49,50</sup> In terms of misorientation angle, the  $\langle 111 \rangle$  38.2° GB has the fastest mobility.<sup>38,39,50</sup> For BCC metals, the GB mobility and its anisotropy are rarely

studied. To the best of the authors' knowledge, only a few GBs in a BCC Fe-20%Cr system,<sup>51</sup> and a  $\Sigma 11$  GB in BCC tungsten<sup>52</sup> were studied with MD simulations. Therefore, it is unclear whether the GB mobility trend observed for FCC metals can be extended to BCC metals.

In this work, MD simulations are conducted to study the GB mobilities in BCC  $\gamma$  U for different rotation axes and misorientations using three interatomic potentials. To the best of the authors' knowledge, this is the first study of GB mobilities of individual GBs as well as GB mobility anisotropy in BCC  $\gamma$  U or U-based alloys, as there are no previous experimental or modeling studies on this topic. The objectives of this work are twofold because this work has both nuclear engineering relevance and is of basic scientific interest. First, the mobilities of a number of GBs in BCC  $\gamma$  U will be calculated so that the results could be used as input for mesoscale fuel performance modeling of grain growth of U-based metallic fuels. This work focuses on pure  $\gamma$  U and the results can be used as references for later studies of GB mobility in U-based alloys. Second, from a fundamental science viewpoint, this work can serve as an attempt to study the general trend of GB mobility anisotropy in BCC metals. In particular, this work seeks to know if the general trend of GB mobility anisotropy for FCC metals (i.e., GB mobility is fastest for the  $\langle 111 \rangle$  rotation axis) also holds for BCC metals. If not, this work will determine which low-index rotation axis typically has the fastest mobility in BCC metals.

## 2. Methods

In this work, GB mobilities of BCC  $\gamma$  U were calculated using the widely used shrinking cylindrical grain method.<sup>53,54</sup> A representative simulation setup that is projected on the X-Y plane is shown in Fig. 1. To generate a cylindrical GB structure, first a U single-crystal slab was created with the Z-axis aligned along the desired rotation axis. Typically, the lengths in the X and Y directions are much longer than that in the Z direction so that the slab has a quasi-2D geometry. The dimensions of different single crystal slabs are listed in Table 1. Next the atoms that were within a radius  $r_{\text{grain}} = 100 \text{ \AA}$  from the center of the slab (measured in the X-Y plane) were rotated along the Z axis by a desired misorientation angle  $\theta$  (see Fig. 1). If the distance between two atoms is less than 70% of the first nearest neighbor distance ( $\sim 2.1 \text{ \AA}$ ) after the rotation, one of them is removed to avoid atom overlap. After the overlapping atoms were removed, the simulation systems contained atoms in the range of 55,340 – 86,550. The structure was then equilibrated at the desired temperature for 20 picoseconds (ps) before beginning the remainder of the simulation. As shown in Fig. 1, the as-created simulation system consists of a cylindrical inner grain (red) and an outer matrix grain (blue). The interface between them is the cylindrical GB, which has a pure tilt character because its rotation axis (i.e., Z axis) is always parallel to the GB plane. It should be noted that no single inclination plane is specified in this method, meaning that the resulting GB mobility is an average over many inclinations for a specific misorientation. In this work, three rotation axes were used ([001], [110], [111]), and three misorientation angles ( $20^\circ$ ,  $30^\circ$ ,  $45^\circ$ ) were examined for each rotation axis. These combinations will be used to investigate how the GB mobility changes with both rotation axis and misorientation in  $\gamma$  U, or more broadly, in BCC metals. For the  $\langle 111 \rangle$  rotation axis, an additional misorientation angle of  $38.2^\circ$  was also studied. This misorientation angle, associated with the  $\Sigma 7$  boundary in FCC metals (e.g., Al), has been found to have the highest (or nearly the highest) migration rate or GB mobility.<sup>39,49,50</sup> While no such similar statement has been made about this GB in BCC metals to the best of the authors' knowledge, it is included here for comparison.

Table 1. Dimensions (in units of Å) of the initial single crystal used to generate GBs for the three rotation axes (in the Z direction) as well as for three interatomic potentials. The crystallographic orientations of the X and Y axes are also shown for completeness.

Rotation axis \ Potential	Z = [001] (X = [100], Y = [010])	Z = [110] (X = [001], Y = [1 $\bar{1}$ 0])	Z = [111] (X = [1 $\bar{1}$ 0], Y = [11 $\bar{2}$ ])
ADP <sup>55</sup>	264.0 × 264.0 × 17.60	264.0 × 248.9 × 24.9	248.8 × 250.0 × 30.5
MEAM <sup>56</sup>	259.7 × 259.7 × 17.30	259.7 × 259.6 × 19.6	259.6 × 263.0 × 18.0
EAM <sup>57</sup>	265.7 × 265.7 × 17.71	265.7 × 250.5 × 25.1	250.5 × 251.6 × 30.7

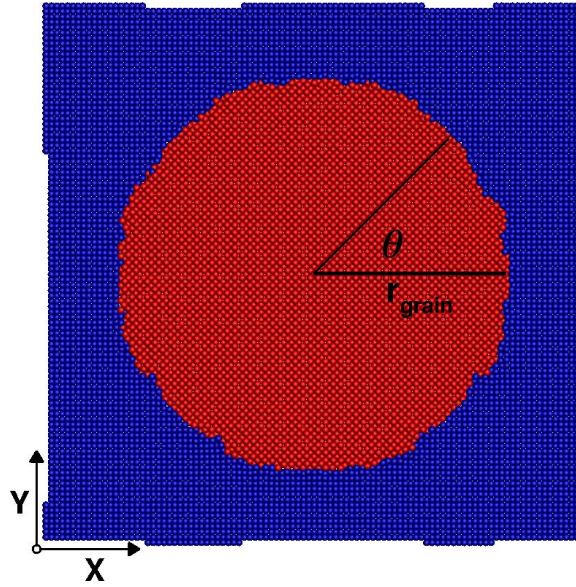


Fig. 1. Schematic of the as-created cylindrical GB structure that is projected on the X-Y plane. The rotation axis is along the Z direction (out of the page). Atoms within the radius  $r_{grain}$  are rotated by a desired misorientation angle  $\theta$ . Red atoms belong to the inner cylindrical grain while blue atoms belong to the outer matrix grain. The interface between them is the cylindrical GB.

At elevated temperatures, the inner grain will shrink due to its positive curvature (equivalently, the outer grain will grow) so that the GB moves inward. From the GB migration velocity, its mobility can be extracted (more details will be provided later in this Section). In this work, the MD method is used to simulate the GB migration. All simulations were conducted using the LAMMPS software.<sup>58</sup> Three different interatomic potentials were used for comparison: an embedded atom method (EAM) potential for the U-Mo-Xe system,<sup>57</sup> an angular dependent potential (ADP) for the U-Mo system,<sup>55</sup> and a modified EAM potential (MEAM) for the pure U system.<sup>56</sup> Although the EAM and ADP potentials are able to model multi-component systems, only the pure U part was used as this work only studies the GB mobilities in pure  $\gamma$  U. Table 2 lists some basic properties predicted by these potentials, such as the lattice parameter of BCC  $\gamma$  U, melting temperature, and the  $\beta \rightarrow \gamma$  phase transition temperature (if applicable). Note that in reality the U phase transition follows  $\alpha \rightarrow \beta \rightarrow \gamma$  as the temperature increases<sup>8,9</sup>. However, in the EAM

and MEAM potentials the  $\beta$  phase is ignored. Therefore, in these cases the  $\alpha \rightarrow \gamma$  transition temperature is given. The experimentally determined values are also listed for comparison. Each of the potentials used in this work had a different focus during its development, which will be described in more detail in the Discussion Section. However, none of them have ever been used to evaluate the GB mobilities. Therefore, this work will elucidate if these potentials predict significantly different GB mobilities. For the EAM and MEAM potentials a temperature range of 1050 – 1400 K was used in calculating the GB mobilities. Since the ADP potential estimates a lower melting point than the other two potentials, a narrower temperature range of 1050 – 1300 K was used. In all simulations, periodic boundary conditions were employed in all three Cartesian directions. All simulations were run using the isobaric-isothermal ensemble (NPT), where the pressure was maintained at zero bars. A time step of two femtoseconds (fs) was used for integration. Snapshots of the atomic structures were saved every 20 ps of simulated time for later analysis.

Table 2. Some basic properties predicted by the three interatomic potentials used in this work, taken from the papers describing their creation. The experimental results are also shown for comparison.

Potential	$\gamma$ U lattice parameter (Å)	$\alpha$ or $\beta \rightarrow \gamma$ transition temperature (K)	Melting point (K)
EAM <sup>57</sup>	3.542 (at 900 K)	< 900 <sup>*</sup>	1530
ADP <sup>55</sup>	3.52 (at 1000 K)	< 1000 <sup>†</sup>	1330
MEAM <sup>56</sup>	3.463 (unknown)	972.5 <sup>‡</sup>	1505.4
Experimental	3.48 (at 1073 K) <sup>59</sup>	1033 <sup>§, 59</sup>	1407 <sup>60</sup>

<sup>\*</sup>Note this potential can predict  $\alpha$  and  $\gamma$ , but not the  $\beta$  phase. However, the  $\alpha \rightarrow \gamma$  transition temperature was not given in the paper either. The authors of this paper indicated that their simulation of  $\gamma$  phase was done at 900 K, indicating an  $\alpha \rightarrow \gamma$  transition temperature below this value.

<sup>†</sup>This potential can describe the  $\alpha$ ,  $\beta$ ,  $\gamma$  and liquid (L) phases of pure U, though only the  $\gamma \rightarrow$  L transition (melting) temperature was given. The lattice parameter of  $\gamma$  U was estimated at 1000 K, so the transition temperature should be lower than that.

<sup>‡</sup>This potential describes the  $\alpha$  and  $\gamma$  phases of pure U, ignoring the  $\beta$  phase. Thus, this is the estimated transition temperature for  $\alpha \rightarrow \gamma$ .

<sup>§</sup>The  $\alpha \rightarrow \beta$  transition occurs at approximately 913 K, and the  $\beta \rightarrow \gamma$  transition occurs at approximately 1033 K.

GB mobility ( $M$ ) is typically assumed to have the following relationship with GB migration velocity ( $v$ ) under a driving force ( $F$ ):<sup>39</sup>

$$v = M \times F. \quad (2)$$

For the cylindrical GBs studied in this work (Fig. 1), the driving force is the ratio of GB energy ( $\gamma$ ) to grain radius ( $R$ ):<sup>39</sup>

$$F = \gamma/R. \quad (3)$$

Therefore, the driving force increases with the decreasing grain radius or with the increasing grain curvature ( $1/R$ ). The GB velocity is the shrinking rate of the cylindrical grain radius:  $v = dR/dt$ . In many previous studies,<sup>40,51,54</sup> a reduced mobility is often used, which is defined as  $M^* = M\gamma$ . Using these equations, Eq. (2) can be rewritten to get a relationship between the reduced GB mobility and the shrinking rate of the cross-sectional area ( $A = \pi R^2$ ) of the cylindrical grain:

$$M^* = \frac{1}{2\pi} \frac{dA}{dt}. \quad (4)$$

The instantaneous cross-sectional area ( $A$ ) at a given time ( $t$ ) can be determined by the number of atoms inside the cylindrical grain. To calculate this, for each snapshot each atom was assigned to either the outer matrix grain or the inner cylindrical grain using the orientation parameter method described by Ulomek *et al.*, which uses diffraction theory to assign an orientation parameter ( $\chi_j$ ) to each atom ( $j$ ) in a grain based on the arrangement of its neighbors in terms of both orientation and regularity.<sup>61</sup> Note that this orientation parameter is an average over each atom's local neighborhood, and it depends on *a priori* knowledge of the grain orientations, and thus cannot be used to calculate the misorientation between grains. A cutoff distance of  $1.2a_0$  (where  $a_0$  is the lattice parameter from Table 2) around each atom was used to determine  $\chi_j$  for each atom. Here if  $\chi_j < 0.0$ , the atom was assigned to the inner grain. Otherwise, it was treated as an atom in the outer matrix grain. Other cutoff distances were also tested, but this one gave the most robust results. For example, the two grains shown in Fig. 1 are an outcome of using this cutoff distance for grain assignment. Figure 2 also demonstrates the robustness of this parameter to temperature fluctuations, when a  $\langle 110 \rangle 45^\circ$  GB is shown at three different times as simulated at 1200 K using the EAM potential.

Once the instantaneous number of atoms ( $N$ ) for the cylindrical (inner) grain was determined for each snapshot, its cross-sectional area was calculated by

$$A = \frac{Na_0^3}{2L_z}, \quad (5)$$

where  $L_z$  is the height of the cylindrical grain in the Z direction and the  $a_0^3/2$  term represents the volume per atom in a BCC crystal. By plotting the cross-sectional area as a function of simulation time, the shrinking rate of the cylindrical grain area, or the slope of the plot ( $dA/dt$ ), can be calculated, which will be used for Eq. (4). An in-house code was used to calculate the slope using a piecewise linear fitting routine.<sup>62</sup> Each area vs. time plot was fit to a maximum of six linear functions; the initial regime was occasionally discounted to allow for further equilibration, and the final linear fit was often to a period of no growth (i.e., the cylindrical grain had completely disappeared). After discarding the linear fits that did not represent the average behavior, a single linear fit was performed over the domain specified by the remaining linear fits. Fig. 3 shows several representative examples of the fitted slopes using this procedure. The grayed-out data points are excluded from the overall fit. Fig. 3(a) shows the area vs. time plot for a  $\langle 100 \rangle 20^\circ$  GB at 1200 K using the ADP potential. In this case, the grain area decreases almost linearly with time so that the slope can be fitted straightforwardly. In most of the simulations, the results have a similar behavior. Fig. 3(b) shows the result of a  $\langle 100 \rangle 20^\circ$  GB at 1050 K using the EAM potential. The initial regime has a slightly different slope from the intermediate regime, and the final regime has rapid grain shrinkage until the grain disappears. Overall, the area decreases nearly linearly with time. Therefore, to get an average rate of the three stages, fits were to the entire growth regime in such simulations. Fig. 3(c) shows the result of a  $\langle 111 \rangle 20^\circ$  GB at 1100 K using the EAM potential.

There was an initial regime of rapid grain shrinkage (for a few tens of picoseconds, shown as the grayed-out data points) followed by a longer regime of slower grain shrinkage. In this case, the initial regime is not included in the fits as it has a distinct behavior from the rest. Fig. 3(d) shows the result of a  $\langle 111 \rangle 30^\circ$  GB at 1250 K using the EAM potential. The grain area does not have a linear decrease with time. This type of behavior was observed when the simulated GBs migrated slowly. Previously, such non-linear behavior was also observed in Cu when the cylindrical grain shrinkage method was used.<sup>54</sup> To avoid bias of selecting the fitting regimes, fits were over all data for these types of results. The results shown in Fig. 3 represent most of the behaviors of the shrinking grain, although sometimes a combination of them exist. Nevertheless, as much shrinking grain data as possible was included in the fits and only some distinctive data was discarded (e.g., the initial stage shown in Fig. 3(c)). In addition, for each simulation condition, three to five independent simulations were conducted to obtain statistically meaningful results, which reduces the unavoidable uncertainties in the fitting. After GB mobilities are obtained at different temperatures, an Arrhenius fit was conducted to obtain the mobility prefactor ( $M_0$ ) and activation energy ( $Q$ ),

$$M^* = M_0 \exp\left(-\frac{Q}{k_B T}\right). \quad (6)$$

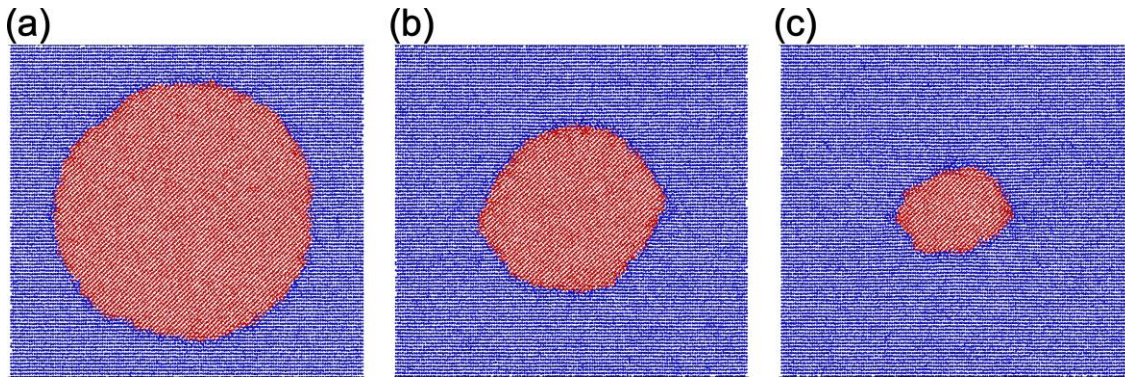


Fig. 2. Example of inner grain shrinkage observed during simulation for a  $\langle 110 \rangle 45^\circ$  boundary using the EAM potential at 1200 K. (a) The initial structure. (b) After 600 ps. (c) After 1000 ps. In all figures red atoms belong to the inner cylindrical grain while blue atoms belong to the outer matrix grain.

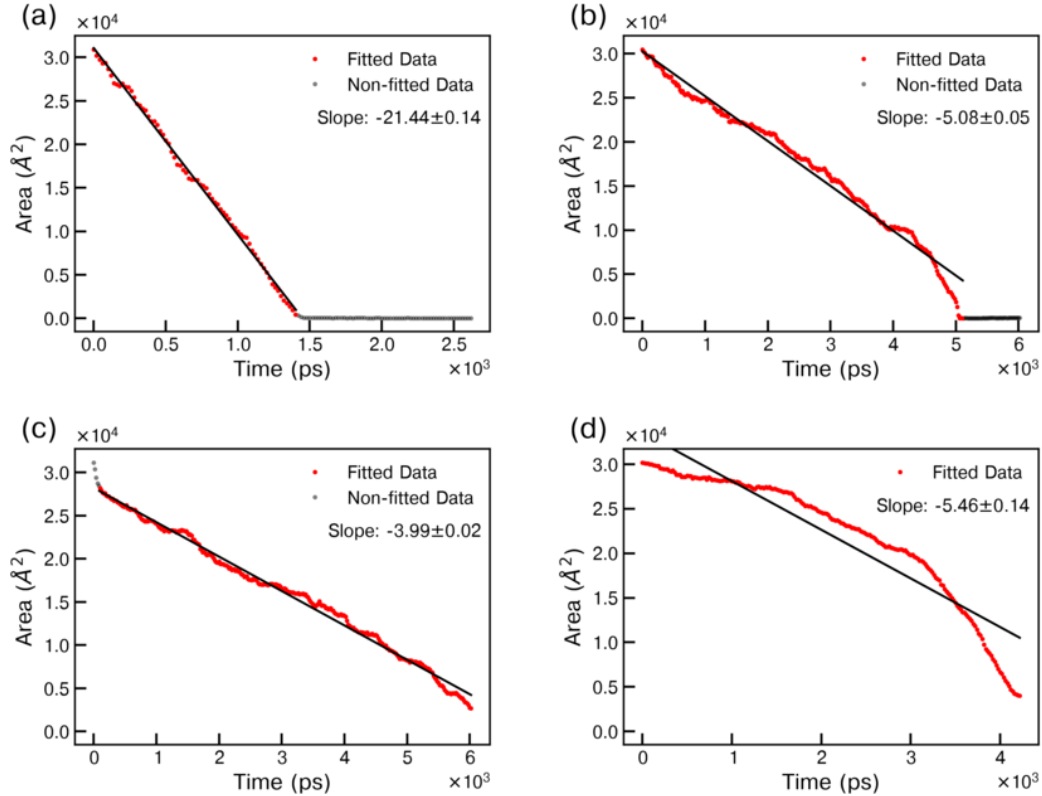


Fig. 3. Four representative examples for fitting the slope ( $dA/dt$ ) from the inner grain area vs. time plot. (a) The  $\langle 100 \rangle$   $20^\circ$  GB at 1200 K using the ADP potential. (b) The  $\langle 100 \rangle$   $20^\circ$  GB at 1050 K using the EAM potential. (c) The  $\langle 111 \rangle$   $20^\circ$  GB at 1100 K using the EAM potential. (d) The  $\langle 111 \rangle$   $30^\circ$  GB at 1250 K using the EAM potential. The solid line is the final fit in each figure. Grayed-out data points are not included in the fit.

Previously, it has been shown that the cylindrical grain can rotate during GB migration in FCC Cu.<sup>54</sup> The rotation can be either clockwise (CW) or counterclockwise (CCW). To investigate if such grain rotation behavior also occurs in BCC  $\gamma$  U, this work has examined the qualitative rotation behavior of the cylindrical grain. This analysis was done by specifying a strip of atoms down the center of the simulation cell consisting of all atoms in the middle 10% along the X direction. These atoms were used as “markers” and tracked through the duration of the simulation. If the strip orientation did not change after the grain shrinks completely (i.e., the strip remained straight as shown in Fig. 4(a)), the grain did not rotate. However, if the strip began twisting in on itself and making an ‘S’ shape, then rotation did occur. The orientation of the ‘S’ shape determines whether the rotation is CW (having a backwards ‘S’ shape as shown in Fig. 4(b)) or CCW (having an ‘S’ shape as shown in Fig. 4(c)). The degree of rotation is unable to be precisely determined using this analysis, so only the qualitative rotation behavior (i.e., CW, CCW, or no rotation) is reported. This analysis was performed for each simulation and the statistics of the grain rotation behavior will be presented in the Results Section.

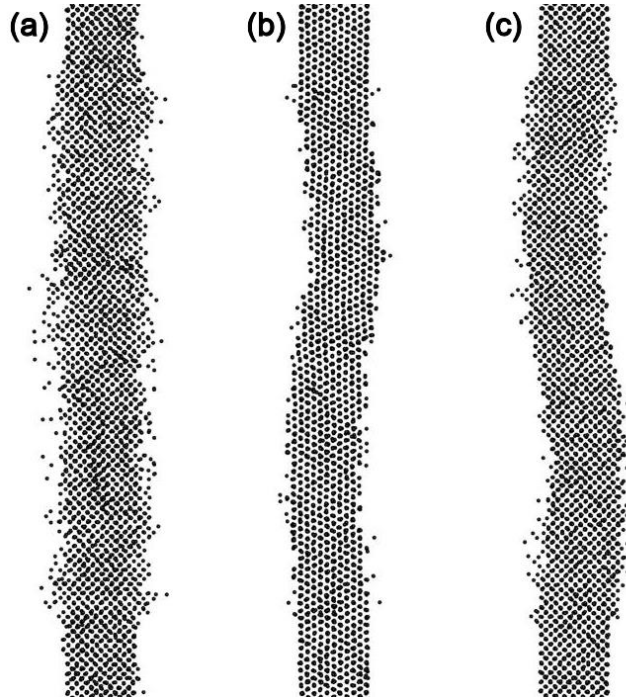


Fig. 4. Representative examples of cylindrical grain rotation observed in this work. All three examples are obtained using the MEAM potential. (a) No rotation observed in the  $\langle 100 \rangle$   $30^\circ$  GB at 1400 K. (b) Clockwise (CW) rotation (indicated by the backwards ‘S’ shape) observed in the  $\langle 111 \rangle$   $45^\circ$  GB at 1050 K. (c) Counterclockwise (CCW) rotation (indicated by the ‘S’ shape) observed in the  $\langle 100 \rangle$   $45^\circ$  GB at 1050 K. Although these examples are taken from the simulations using the MEAM potential, the other two potentials also demonstrated these behaviors.

### 3. Results

GB mobility results are presented first by each rotation axis with different misorientation angles as predicted by different potentials. These results will elucidate if GB mobility in BCC  $\gamma$  U has a clear correlation with the misorientation angle. Next, these mobilities are compared at the same misorientation angle but with different rotation axes to identify if GB mobility in BCC  $\gamma$  U has a general trend with the rotation axis, like in the FCC metals (i.e.,  $\langle 111 \rangle$  rotation axis may have a faster mobility than  $\langle 100 \rangle$  and  $\langle 110 \rangle$  in FCC metals<sup>39</sup>). Finally, the statistics of grain rotation behavior are presented to explore possible trends, if any.

#### 3.1. $\langle 100 \rangle$ mobility trends

The GB mobilities for the  $\langle 100 \rangle$  rotation axis at three misorientation angles predicted by the EAM potential are shown in Fig. 5(a), which is an Arrhenius plot. In the temperature range studied (1050 K – 1400 K), overall, the mobility from slowest to fastest is  $45^\circ < 20^\circ < 30^\circ$ . Therefore, the mobility does not increase or decrease monotonically with increasing misorientation angle. The mobilities of each of the  $30^\circ$  and  $45^\circ$  GBs can be well fitted by an Arrhenius relationship. However, it seems that the  $20^\circ$  boundary does not have a normal Arrhenius-type temperature dependence, having a step that looks like athermal behavior (i.e., mobility does not change with temperature) in the temperature range of 1200 K – 1300 K. It is unclear if a different mechanism drives the grain growth behavior in this temperature range, as the mechanisms for anti-

thermal (i.e., mobility decreases with the increasing temperature) or athermal GB motion are largely unknown.<sup>63</sup> On the other hand, this athermal behavior could be due to the insufficient statistics of GB mobility calculations. If the two temperature ranges above and below this athermal region are treated separately, the activation energy and prefactor for an Arrhenius fit in the temperature range of 1050 – 1200 K are 0.7 eV and  $20.9 \times 10^{-6}$  m<sup>2</sup>/s, and for the temperature range of 1300 – 1400 K, they are 0.6 eV and  $5.8 \times 10^{-6}$  m<sup>2</sup>/s. If an Arrhenius behavior is assumed for the whole temperature range of 1050 – 1400 K, the values are 0.31 eV and  $421.3 \times 10^{-9}$  m<sup>2</sup>/s, which are shown in Table 3.

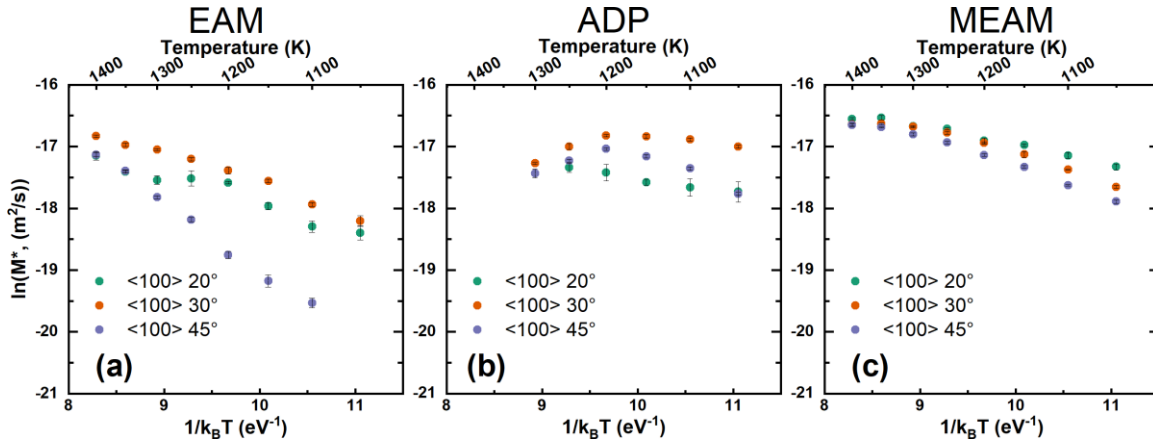


Fig. 5. Calculated GB mobilities (displayed as Arrhenius plots) for the  $\langle 100 \rangle$  rotation axis with three misorientation angles ( $20^\circ$ ,  $30^\circ$ ,  $45^\circ$ ) using the (a) EAM potential, (b) ADP potential, and (c) MEAM potential. Each data point is averaged over three to five independent simulations. Error bars represent standard error. Note that in each figure the bottom axis is  $1/(k_B T)$ , while the top axis shows the absolute temperature on a reversed scale (temperature decreases from left to right).

For a GB to migrate, atoms need to diffuse across the GB plane according to Burke and Turnbull's theory.<sup>64</sup> Therefore, atomic motion in the X and Y directions as shown in Fig. 1, which are both perpendicular to the GB plane, should contribute to GB motion directly. On the other hand, atomic motion in the direction parallel to the GB plane, which is the Z direction in Fig. 1, might not contribute to the GB motion significantly. To check this hypothesis, the mean square displacements (MSDs) of all atoms are tracked during GB motion.

Fig. 6 shows the MSD plots for the  $[001]$  rotation axis with  $20^\circ$ ,  $30^\circ$ , and  $45^\circ$  misorientation angles at 1100 K predicted by the EAM potential. In all plots, the MSDs along the X and Y directions (i.e., across the GB plane) are approximately equal. This is consistent with the nearly circular shrinking behavior of the inner grain during GB motion (Fig. 2). The  $20^\circ$  boundary (

Fig. 6(a)) overall appears to have relatively equal motion in all three Cartesian directions, although the X direction has a slightly larger MSD at the end of simulation. For the  $30^\circ$  boundary (

Fig. 6(b)), it has slightly more atomic motion in the Z direction than the other two, which is parallel to the GB plane (also the rotation axis direction). The MSD of the  $45^\circ$  boundary (

Fig. 6(c)) shows atomic motion primarily along the Z direction (i.e., parallel to the GB plane), the magnitude of which is significantly more than both the 20° and 30° boundaries. The MSDs in the X and Y directions seem to be congruent, but the zoom-in view shows that they are not identical (see the inset of

Fig. 6(c)). From Fig. 5(a), the 45° boundary has the lowest mobility. Therefore, the MSD behavior is consistent with the above hypothesis that the atomic motion parallel to the GB plane might not contribute to GB motion significantly. In other words, if atomic motion is primarily parallel to the GB plane, the GB mobility is likely to be slow. Regarding the aforementioned athermal behavior of the <100> 20° GB between 1200 K – 1300 K (Fig. 5a), the MSDs were also examined. The MSDs in the X, Y, and Z directions (not shown) in this temperature range are all nearly equivalent (similar to Fig. 6a, which is not in the athermal regime). Therefore, the MSD behavior is unable to explain why the athermal region appears.

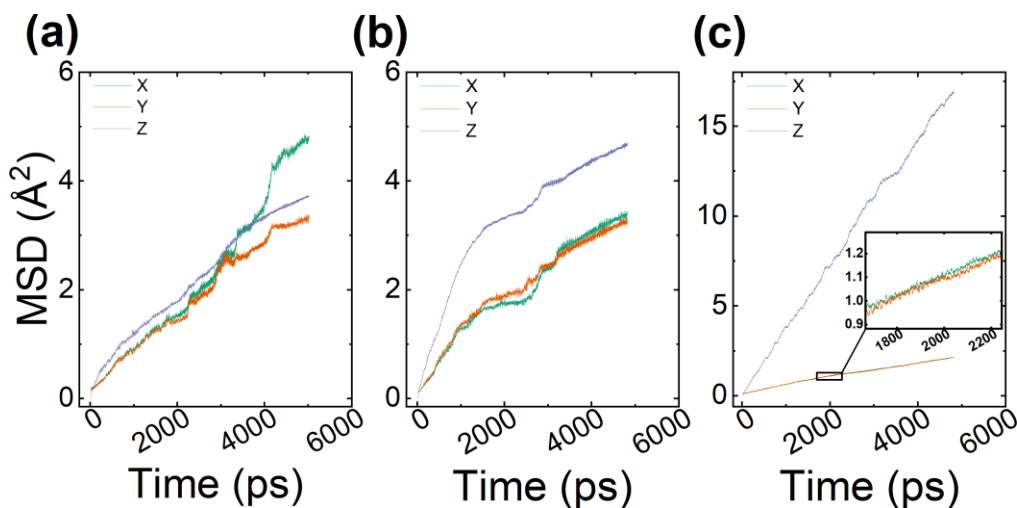


Fig. 6. MSDs for the [001] rotation axis with three misorientation angles at 1100 K predicted by the EAM potential. (a) 20°. (b) 30°. (c) 45°. Note that in (c) the vertical (ordinate) axis has a different scale than in (a) and (b).

Table 3. Activation energies and GB mobility prefactors predicted by the EAM potential. Activation energies ( $Q$ ) are given in  $eV$ , and the prefactors ( $M_0$ ) are given in  $m^2/s \times 10^{-9}$ .

Rotation axis Misorientation	<100>		<110>		<111>	
	$Q$	$M_0$	$Q$	$M_0$	$Q$	$M_0$
20°	0.31	421.3	0.29	848.3	0.88	93,300
30°	0.46	2400	0.48	3200	1.05	236,400
45°	1.12	426,500	0.42	2000	0.92	118,600
38.2°	—	—	—	—	0.93	107,300

For the ADP potential, the GB mobility trend of the <100> rotation axis is 20° < 45° < 30° (Fig. 5(b)), although the differences are small. The 20° boundary structure completely melted at

1300 K, so no mobility data are available at this temperature. Significant GB pre-melting occurred for the 30° and 45° boundaries at this temperature as well, but the melt did not fully overtake the simulated domain. This is consistent with the original description of the ADP potential with a melting point of 1330 K.<sup>55</sup> The premelting behavior depends on the GB type, which is similar to GB premelting in other systems such as Ni.<sup>65</sup> Above 1200 K there is a decrease in the GB mobility with increasing temperature (or “anti-thermal” behavior), which is likely associated with GB premelting in these simulations. With the presence of the melt at the GB, the orientation parameter does not accurately identify the position of the GB plane, further contributing to the uncertainty of GB mobility calculations of this anti-thermal regime. Therefore, the Arrhenius fits were only conducted in the temperature range of 1050 – 1200 K, and the extracted GB mobility values are listed in Table 4. For the MSD plots (not shown), in general the three directions have similar values for each misorientation angle, with the Z direction sometimes having a slightly larger value (similar to

Fig. 6(a) and (b)). From Fig. 5(b), it can be seen that the GB mobilities are similar for the three misorientations and they are relatively fast in comparison with their counterparts in the EAM potential (Fig. 5(a)). Therefore, again the MSD behavior is consistent with the mobility trend.

Table 4. Activation energies and GB mobility prefactors predicted by the ADP potential. Activation energies ( $Q$ ) are given in  $eV$ , and the prefactors ( $M_0$ ) in  $m^2/s \times 10^{-9}$ .

Rotation axis \ Misorientation	<100>		<110>		<111>	
	$Q$	$M_0$	$Q$	$M_0$	$Q$	$M_0$
20°	0.21	199.0	0.22	530.2	0.16	282.4
30°	0.12	156.5	0.14	187.4	0.37	1600
45°	0.51	5600	0.11	140.2	0.19	288.1
38.2°	—	—	—	—	0.33	956.5

The mobility trend predicted by the MEAM potential for the <100> rotation axis is 45° < 30° < 20° (Fig. 5(c)), but the differences between misorientations are very small. As the temperature increases, the differences vanish and converge to nearly a single value at 1400 K. All three misorientations follow Arrhenius behavior well, and the extracted activation energies and GB mobility prefactors are listed in Table 5. In general, the MSD behavior (not shown) shows that the atomic motion is similar in the three directions, though the Z direction is higher only by a small margin (similar to

Fig. 6(b)). However, this is not true for the 20° misorientation, where the MSD in the Z direction is slightly lower than the other two directions from 1050 K to 1300 K. Since the atomic motion across the GB (i.e., in the X and Y directions) contributes directly to the GB motion, the MSD behavior is consistent with the fact that the 20° boundary is the fastest one among the three misorientations.

Table 5. Activation energies and GB mobility prefactors predicted by the MEAM potential. Activation energies ( $Q$ ) are given in  $eV$ , and the prefactors ( $M_0$ ) in  $m^2/s \times 10^{-9}$ .

Rotation axis Misorientation	<100>		<110>		<111>	
	$Q$	$M_0$	$Q$	$M_0$	$Q$	$M_0$
20°	0.26	580.1	0.17	279.6	0.32	1000
30°	0.39	1700	0.24	616.0	0.22	438.5
45°	0.47	3100	0.21	421.3	0.26	557.4
38.2°	—	—	—	—	0.18	250.5

### 3.2. <110> mobility trends

The GB mobility trend of the <110> rotation axis predicted by the EAM potential is  $30^\circ \approx 45^\circ < 20^\circ$  (Fig. 7a), which is different from that of the <100> axis (Fig. 5(a)). At the highest temperature (1400 K), the mobility appears to converge to nearly a single value. There is a slight curvature in the Arrhenius plot for the  $20^\circ$  boundary, potentially<sup>66</sup> indicating the presence of multiple activated behaviors with a smooth transition between the preferred mechanisms with temperature.<sup>67</sup> However, a linear fit still fits the data well for this boundary as well as for the other two GBs. The extracted activation energies and prefactors for this rotation axis are listed in Table 3. Examining the MSD data (not shown) reveals that the  $20^\circ$  boundary has more atomic motion across the GB (in the X and Y directions) than that parallel to the GB (in the Z direction) at all temperatures except at 1400 K. For the  $30^\circ$  and  $45^\circ$  boundaries, the atomic motion is nearly equivalent in all three Cartesian directions. Therefore, the MSD behavior is consistent with the mobility trend (i.e., the  $20^\circ$  boundary is the fastest one). At 1400 K, the MSD for all misorientations as well as all directions were nearly equal. This behavior explains why the three boundaries have nearly the same mobility at this temperature.

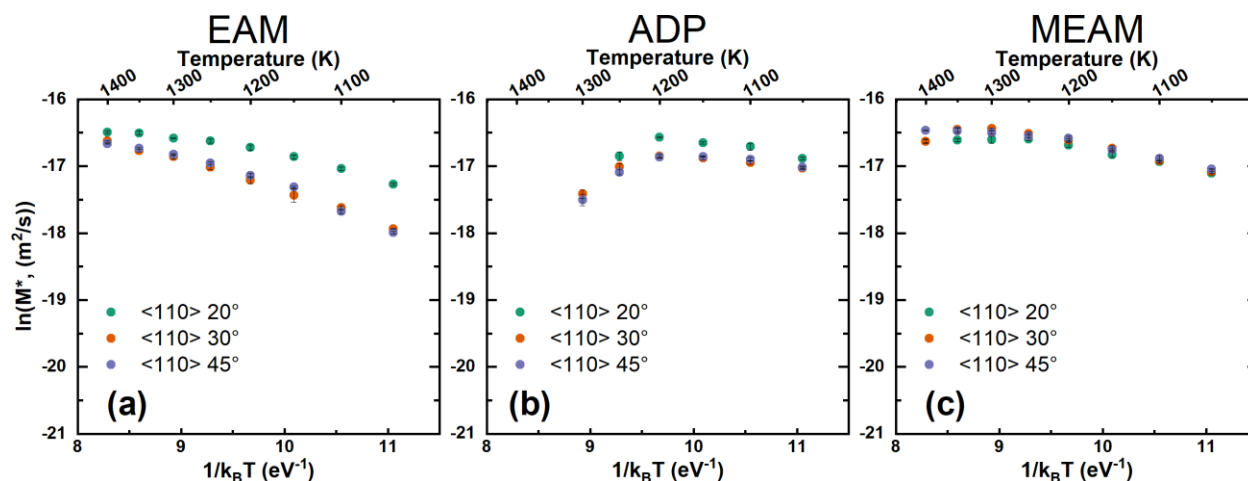


Fig. 7. Calculated GB mobilities (displayed as Arrhenius plots) for the <110> rotation axis with three misorientation angles ( $20^\circ$ ,  $30^\circ$ ,  $45^\circ$ ) using the (a) EAM potential, (b) ADP potential, and (c) MEAM potential. Each data point is averaged over three to five independent simulations. Error bars represent standard error. Note that in each figure the bottom axis is  $1/(k_B T)$ , while the top axis shows the absolute temperature on a reversed scale (temperature decreases from left to right).

For the  $\langle 110 \rangle$  rotation axis using the ADP potential, in terms of the misorientation dependence, the GB mobility order is the same as that using the EAM potential:  $30^\circ \approx 45^\circ < 20^\circ$  (see Fig. 7(b)). As for the temperature dependence, the mobility behaviors are the same as the  $\langle 100 \rangle$  rotation axis for this ADP potential, i.e., they exhibit an anti-thermal regime at temperatures above 1200 K, where the mobility decreases as the temperature increases. Similar to the  $\langle 100 \rangle$  rotation axis, the  $20^\circ$  misorientation experienced issues at 1300 K: although the structure did not completely melt, the melted interface expanded enough to prevent any meaningful calculation of the GB mobility. Therefore, no mobility is reported for this  $20^\circ$  boundary at 1300 K in Fig. 7(b). The  $30^\circ$  and  $45^\circ$  boundaries also experienced significant GB premelting, but a mobility value was still able to be extracted. The anti-thermal regime between 1200 – 1300 K is once again attributed to the GB premelting, as for the  $\langle 100 \rangle$  rotation axis (Fig. 5(b)). Excluding the anti-thermal regime in the Arrhenius fit, the extracted activation energies and GB mobility prefactors are shown in Table 4. The MSD data (not shown) corroborates the mobility trend. The  $20^\circ$  boundary has the highest magnitude of atomic motion in the two directions perpendicular to (i.e., across) the GB plane (X and Y directions) than the other two boundaries. This is consistent with the GB mobility trend that the  $20^\circ$  boundary has the highest mobility. For this boundary, initially the MSD in the X and Y directions are higher than or similar to the Z direction in the temperature range of 1050 – 1200 K. However, when GB premelting occurs and GB mobility drops at 1250 K, the MSD in the Z direction is higher than in the other two directions. This behavior again proves that if the atomic motion is predominant in the direction parallel to the GB plane (Z direction), like in

Fig. 6(c), the GB mobility is slow. For the  $30^\circ$  and  $45^\circ$  boundaries, the MSDs are roughly the same in all three directions from 1050 K to 1200 K. At 1250 K and 1300 K, the MSD in the Z direction is slightly higher (again it is consistent with the mobility drop), possibly due to the GB premelting.

The mobility trend of the misorientation dependence for the MEAM potential is not as clear-cut as the other two potentials for this  $\langle 110 \rangle$  rotation axis (see Fig. 7(c), activation energies and prefactors in Table 5). Across the entire temperature range the mobilities are almost equal for all three misorientations. Examining the MSD plots (not shown) reveals that the  $20^\circ$  boundary has faster atomic motion in the X and Y directions than in the Z direction in the temperature range of 1050 – 1300 K, while the  $30^\circ$  and  $45^\circ$  boundaries have nearly the same MSD in all three directions throughout the whole simulated temperature range. Comparing the three misorientations, the MSDs in the X and Y directions (across the boundary) of the  $20^\circ$  misorientation are higher than its counterparts until about 1300 K. Interestingly, the  $20^\circ$  boundary does not have a higher GB mobility, which is different from other systems as discussed earlier. In general, it appears that the mobility is strongly correlated with atomic motion perpendicular to the GB plane. However, additional factors may still play a role (at least for this potential or the individual boundaries) to either slow down the  $20^\circ$  boundary or speed up the other two boundaries.

### 3.3. $\langle 111 \rangle$ mobility trends

The EAM potential has a general mobility trend of  $30^\circ < 45^\circ < 38.2^\circ < 20^\circ$  (see Fig. 8(a)) for the  $\langle 111 \rangle$  rotation axis, although at lower temperatures ( $\leq 1150$  K) the  $38.2^\circ$  boundary has a slightly higher mobility than the  $20^\circ$  boundary. For the  $30^\circ$  boundary, the GB did not move significantly at temperatures below 1250 K, so no mobility data was reported below this temperature. Each misorientation has some nonlinearity or curvature in the Arrhenius plot. This

could be indicative of a Vogel-Fulcher type of temperature dependence for GB mobility because the atom diffusion and structural relaxation at GBs could be similar to glass forming liquids, as suggested by Zhang et al.<sup>68</sup> The nonlinearity could also be an outcome of separate regimes where different mechanisms dominate. For example, some literature shows that there can be different mechanistic regimes (e.g., a diffusional, or slow-moving regime, where the boundary motion is due to occasional and thermally activated atomic jumps, and a ballistic, or fast-moving regime, where the boundary motion is due to the rapid displacement of atoms<sup>69,70</sup>) having very different activation energies and prefactors, though the transitions between different regimes are sharp, rather than the gradual change observed here. The determining factors for which regime a boundary falls into is the driving force and temperature, with the diffusional regime associated with low driving forces and temperatures, and the ballistic regime associated with high driving forces and temperatures. Strontium titanate ( $\text{SrTiO}_3$ ) has also been found to have an odd temperature dependence of GB mobility with an anti-thermal regime (i.e., the mobility decreases as the temperature increases),<sup>71</sup> thought to be associated with the coexistence of two different types of GBs of different space charge segregations. Therefore, many factors could cause the non-Arrhenius behavior of GB mobility so that the root cause of the nonlinear behavior in this system is not clear. Here, an Arrhenius fit is still used across the entire temperature range to extract the activation energies and mobility prefactors (see Table 3), because the curvature is not very large. At most temperatures, the MSDs of these boundaries (not shown) reveal that the preferred atomic direction is the Z ([111]) direction, parallel to the GB plane. This is indicative that these GBs may have relatively low mobilities, which is consistent with Fig. 8(a). The  $20^\circ$  boundary at 1200 K and the  $30^\circ$  boundary at 1300 K show that the atomic motion in the X and Y directions (across the GB) becomes equal to the motion in the Z direction, staying nearly equal at higher temperatures. The MSD trends share some characteristics that the mobility trend exhibits, but there are some discrepancies as well, as described previously. This indicates that atomic diffusion behavior alone may not be sufficient to predict GB mobility trends for this potential.

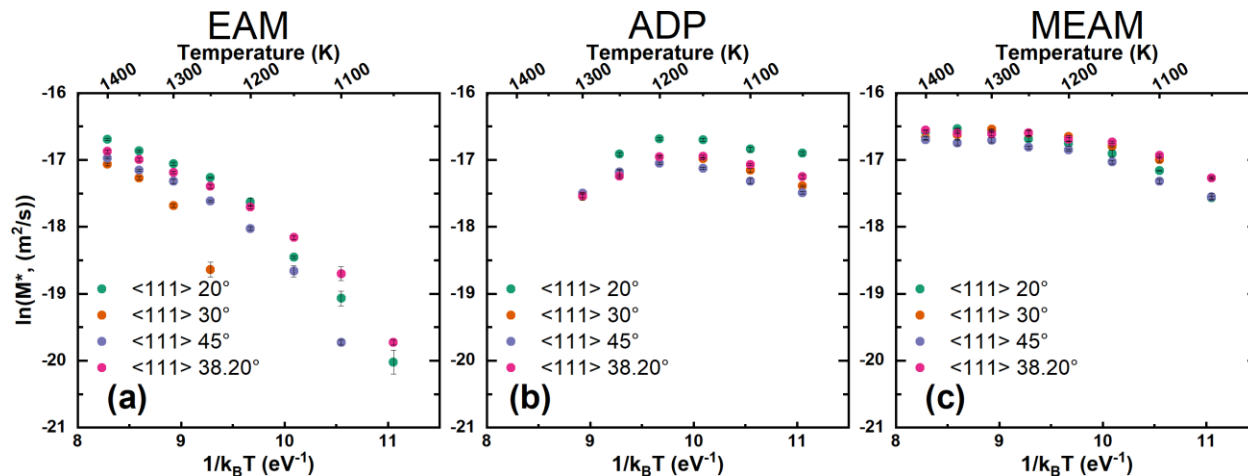


Fig. 8. Calculated GB mobilities (displayed as Arrhenius plots) for the  $\langle 111 \rangle$  rotation axis with four misorientation angles ( $20^\circ$ ,  $30^\circ$ ,  $38.2^\circ$ ,  $45^\circ$ ) using the (a) EAM potential, (b) ADP potential, and (c) MEAM potential. Each data point is averaged over three to five independent simulations. Error bars represent standard error. Note that in each figure the bottom axis is  $1/(k_B T)$ , while the top axis shows the absolute temperature on a reversed scale (temperature decreases from left to right).

For the  $\langle 111 \rangle$  rotation axis using the ADP potential, the trend is  $45^\circ < 30^\circ < 38.2^\circ < 20^\circ$  (Fig. 8(b)). The differences between the  $30^\circ$ ,  $38.2^\circ$ , and  $45^\circ$  boundaries are quite small, while the  $20^\circ$  boundary has a clear margin over other boundaries. The overall temperature dependence is similar to the  $\langle 100 \rangle$  and  $\langle 110 \rangle$  rotation axes using the same ADP potential (Fig. 5(b) and Fig. 7(b)), i.e., there is an anti-thermal regime above 1200 K where the mobility decreases with increasing temperature. Once again, for the  $20^\circ$  boundary at 1300 K, the GB structure melted completely. There was a significant amount of GB premelting for the other three boundaries as well, but the structure did not completely melt. To extract the activation energies and prefactors (listed in Table 4), only the mobility data below 1200 K are included in the Arrhenius fit. For the MSD behaviors of these GBs (not shown), typically the atomic motion in the Z direction (parallel to the GB) dominates (partially due to the pre-melting behavior at high temperatures), except for the  $20^\circ$  and  $30^\circ$  at very low temperatures.

The GB mobility of the MEAM potential using the  $\langle 111 \rangle$  rotation axis does not appear to have significant differences between the four misorientation angles (see Fig. 8(c)), which is similar to the  $\langle 110 \rangle$  rotation axis using the same potential (Fig. 7(c)). At high temperatures (above 1250 K), the GB mobility seems to have an athermal region, where mobility does not change much with the increasing temperature. Table 5 lists the activation energies and mobility prefactors based on an Arrhenius fit across all temperatures. Even though the differences in mobility between these boundaries are small, the  $45^\circ$  boundary is consistently the slowest of the four, while the  $38.2^\circ$  boundary tends to be the fastest. For the MSD behavior (not shown), typically the atomic motion in all three directions is similar at low temperatures while the Z direction ( $[111]$ ) becomes dominant at high temperatures. The  $20^\circ$  boundary with this potential has a different MSD behavior: it has slower atomic motion in the Z direction at temperatures below 1250 K then the trend is reversed. However, the MSD behaviors of these boundaries cannot be correlated to their GB mobilities.

Overall, for each rotation axis, the GB mobility shows some anisotropy with the misorientation angle. However, the anisotropy trend strongly depends on each potential. For most cases, the  $20^\circ$  misorientation has the fastest or similar mobility compared to the other misorientations. The  $\langle 111 \rangle$   $38.2^\circ$  GB, which is the fastest one in FCC metals, is not always the fastest among the four boundaries studied, although it is close to the fastest one if it is not. The MSD behavior sometimes is consistent with the GB mobility trend. For example, if the MSD or atomic motion in the Z direction (parallel to the GB plane) is much higher than the other two directions (perpendicular to the GB plane), the GB mobility is typically low as atomic motion in that direction may not contribute to the GB motion directly.

### 3.4. Mobility trends between different rotation axes

By fixing the misorientation angle it is possible to examine the anisotropy within the rotation axis degrees of freedom. Here the mobility data reported in Figs. 5, 7, and 8 are rearranged to study the anisotropy related to the rotation axis, as shown in Fig. 9. Each figure of Fig. 9 shows the GB mobility anisotropy for the same misorientation angle but with different rotation axis for a specific potential. Some literature identifies that in general the  $\langle 111 \rangle$  rotation axis has higher mobilities than  $\langle 100 \rangle$  and  $\langle 110 \rangle$  axes in FCC metals (e.g., Al), and the highest mobility is around the  $\langle 111 \rangle$   $40^\circ$  GB.<sup>39,49</sup> However, no statements on the mobility anisotropy in BCC metals have been made to the best of the authors' knowledge. Fig. 9 shows that, in BCC U, the  $\langle 110 \rangle$  rotation

axis tends to be the fastest out of the three rotation axes examined. The EAM potential is the most consistent in this regard (Fig. 9(a, d, g)). For the ADP and MEAM potentials, the  $\langle 110 \rangle$  rotation axis is or at least close to the fastest. For the  $\langle 100 \rangle$  axis, it has a greater tendency to be the slowest rotation axis in many cases (Fig. 9(b, f – i)), although sometimes it can be close to the fastest axis (Fig. 9(c – e)). The  $\langle 111 \rangle$  rotation axis fluctuates significantly, but it never becomes the fastest one. The MEAM potential has the most consistent anisotropy trend out of the three potentials in terms of the rotation axis dependence, which is  $M_{110} > M_{111} > M_{100}$ . However, this potential also gives the least amount of variability among the rotation axes.

An analysis of the mobilities of nearly 400 GBs in FCC Ni found that most GB mobilities will converge to a single value near the melting temperature, regardless of the temperature-dependence trend in mobility of these GBs (e.g., thermally activated, athermal, anti-thermal).<sup>72</sup> In this work, this convergence at high temperatures was observed in the ADP and MEAM potentials across all boundaries with a fair degree of reliability (Figs. 9(b, c, e, f, h, i)). For the EAM potential, however, the mobilities did not converge to a single value at high temperatures (Figs. 9(a, d, g)). One possible explanation for this behavior is that the highest temperature studied for the EAM potential is not close enough to its melting or premelting temperature. This is consistent with the fact that the EAM potential has the highest melting temperature among the three potentials (Table 2). This is also consistent with the non-existence of an athermal or anti-thermal regime at high temperatures for the EAM potential (unlike the other two potentials).

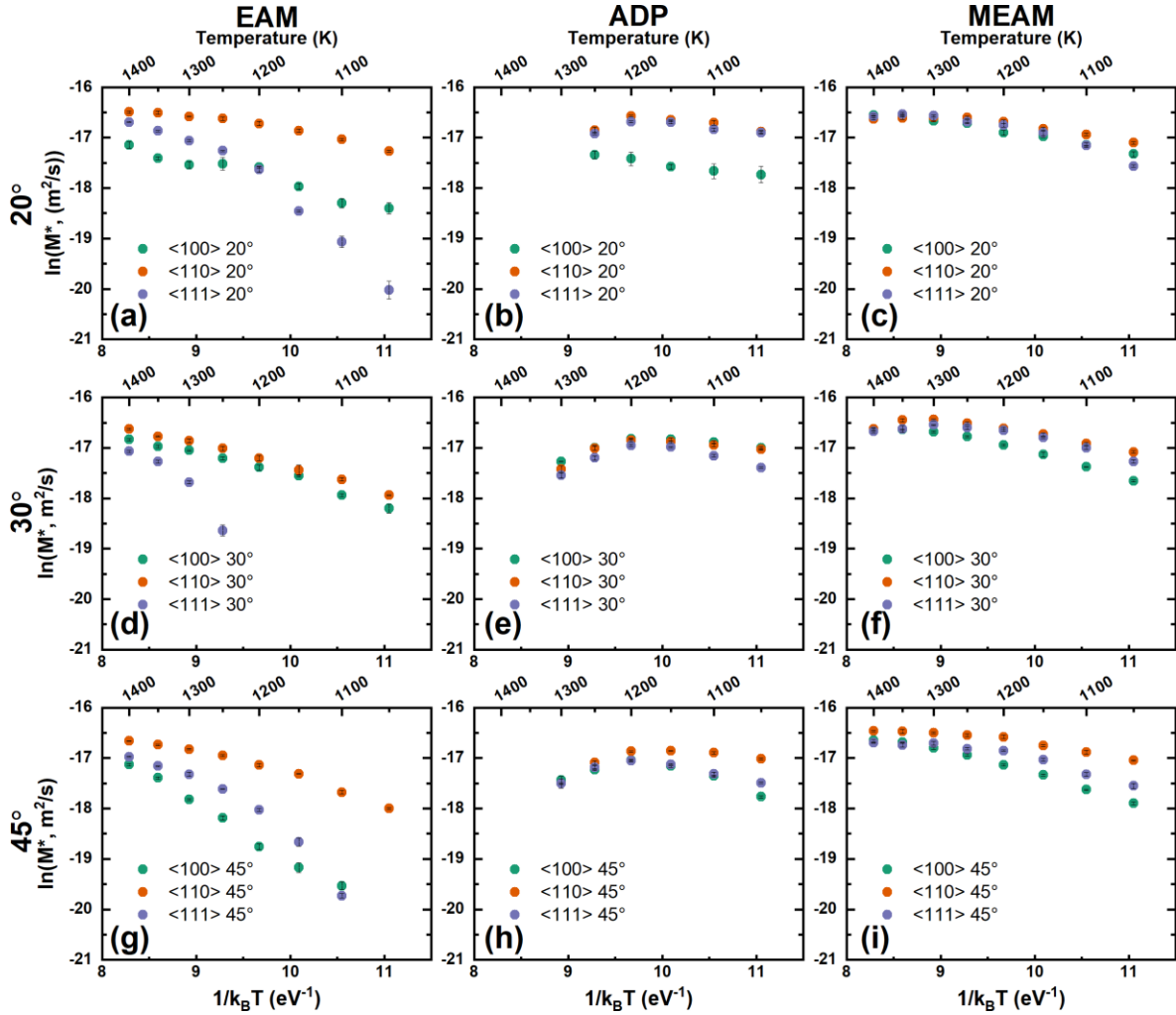


Fig. 9. Arrhenius plot of GB mobilities displayed by different rotation axes with a fixed misorientation and a specific potential in each figure. Each row shows a misorientation while each column shows a potential. Each mobility is averaged over three to five independent simulations. Error bars show the standard error. Note that in each figure the bottom axis is  $1/(k_B T)$ , while the top axis shows the absolute temperature on a reversed scale (temperature decreases from left to right).

### 3.5. Grain rotation behavior

During the simulations, the inner grain (see Fig. 1) was sometimes observed to rotate while it was shrinking. The rotation behavior was either CW, CCW, or stationary, as shown in Fig. 4. In other systems, grain rotation has been observed both experimentally and computationally (see Ref. <sup>54</sup> and references therein). Grains will rotate to drive the free energy of the system down by (typically) creating a new GB with a lower GB energy. Grain rotation is not universally observed though, meaning that additional factors also govern the grain rotation. For a more in-depth discussion of grain rotation and possible reasons for not rotating, see Ref. <sup>54</sup>. This work examined the qualitative rotation behavior for each simulation. Fig. 10 – Fig. 12 show the percentages of all

simulations that rotated either CW, CCW, or had no observable rotation for the three potentials respectively. The EAM potential (Fig. 10) across all simulations tended to have no rotation (74.85%). A majority of the remainder of the simulations had CCW (18.4%), while the CW rotation is only 6.75%. For individual GBs (i.e., a rotation axis and misorientation pair), the predominant rotation behavior was to not rotate, though the  $\langle 110 \rangle 20^\circ$  has a predominant CCW rotation. For those GBs with mixed rotation behavior (e.g.,  $\langle 100 \rangle 45^\circ$ ), the rotation direction is stochastic and does not depend on the temperature. Through cross comparisons between different rotation axes and misorientations, no clear trend can be identified. For the ADP potential (Fig. 11), again the majority of GBs (60%) had no rotation, although the percentage is lower than that for the EAM potential. The percentages of CCW (26.27%) and CW (13.73%) are higher than its counterparts of the EAM potential. All GBs have a mixed rotation behavior; all except the  $\langle 110 \rangle 45^\circ$  GB have all three rotation behaviors. Again, no clear trend can be identified in terms of rotation axis or misorientation dependence. For the MEAM potential (Fig. 12), the majority of GBs had no rotation (55.15%), followed by CCW (34.93%) and CW (9.93%) rotation. Most individual GBs also had a mixed rotation behavior, although many of them only had two rotation behaviors.

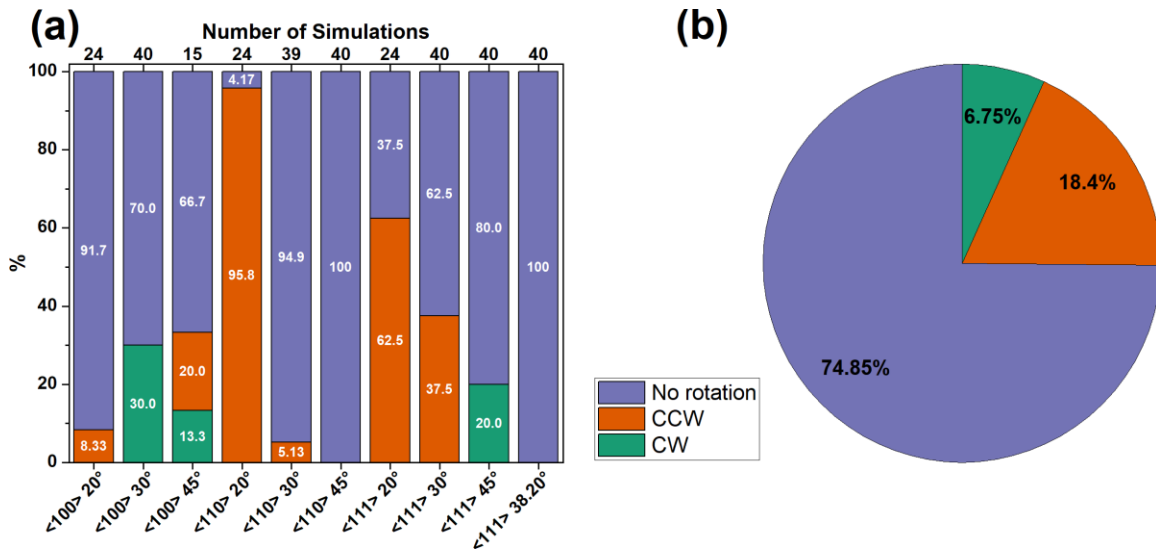


Fig. 10. Summary of the grain rotation behavior for simulations using the EAM potential, showing the percentage of simulations that underwent no rotation, counterclockwise (CCW) rotation, and clockwise (CW) rotation. (a) By GB type (bottom axis). The top axis indicates the number of simulations for each GB. (b) Overall statistics. Note that for the  $\langle 100 \rangle 45^\circ$  boundary only 15 simulations were analyzed here, because the grain growth was very limited at temperatures below 1300 K and the grain rotation behavior could not be unambiguously determined.

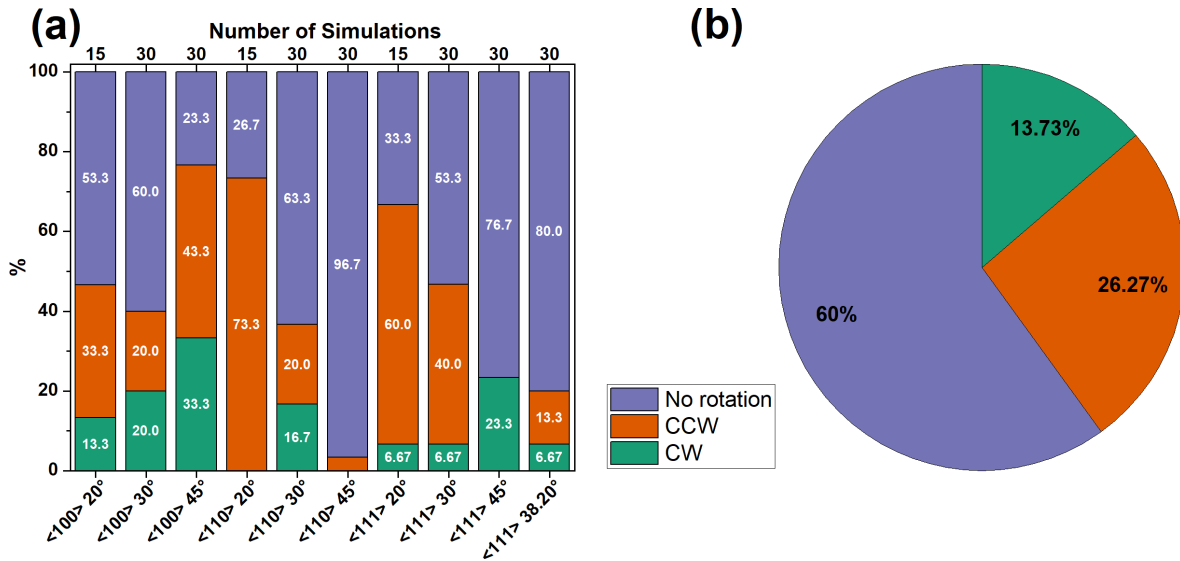


Fig. 11. Summary of the grain rotation behavior for simulations using the ADP potential, showing the percentage of simulations that underwent no rotation, counterclockwise (CCW) rotation, and clockwise (CW) rotation. (a) By GB type (bottom axis). The top axis indicates the number of simulations for each GB. (b) Overall statistics.

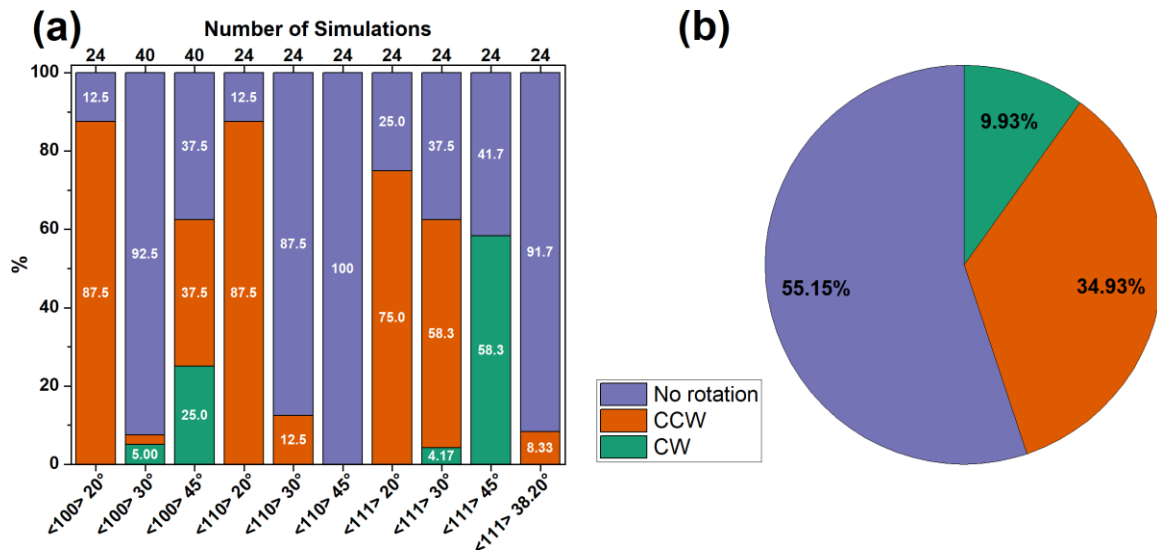


Fig. 12. Summary of the grain rotation behavior for simulations using the MEAM potential, showing the percentage of simulations that underwent no rotation, counterclockwise (CCW) rotation, and clockwise (CW) rotation. (a) By GB type (bottom axis). The top axis indicates the number of simulations for each GB. (b) Overall statistics.

At high temperatures (near the melting point of the material), grain rotation is not expected to happen due to the disappearance of the coupling factor between normal and tangential boundary velocity, which occurs when the GB premelts.<sup>54</sup> Trautt and Mishin found in their simulations on FCC Cu that grain rotation ceased when the temperature rose above 80% of the melting temperature.<sup>54</sup> In this work, only the ADP potential underwent GB premelting, and in most cases there was no grain rotation observed. However, some rotation was still observed at these elevated temperatures (see Fig. 13). Even in the presence of the GB melt, nearly 50% of the simulations at 1300 K and over 20% at 1250 K for the ADP potential demonstrated some grain rotation. If the trend of grain rotation ceasing is consistent between FCC Cu and BCC U, the expected temperatures (80% of the melting temperature) at which grain rotation ceases would be ~1225 K for the EAM potential, ~1060 K for the ADP potential, and ~1200 K for the MEAM potential. As shown in Fig. 13, this clearly is not the case, as grain rotation is observed across the whole simulated temperature range. Therefore, grain rotation has been observed at high temperatures in this work, which is different from the no rotation behavior observed in Cu by Trautt et al.<sup>54</sup> at high temperatures. The cause of grain rotation at these elevated temperatures where (presumably) the coupling factor between the normal and tangential velocities is zero remains unknown.

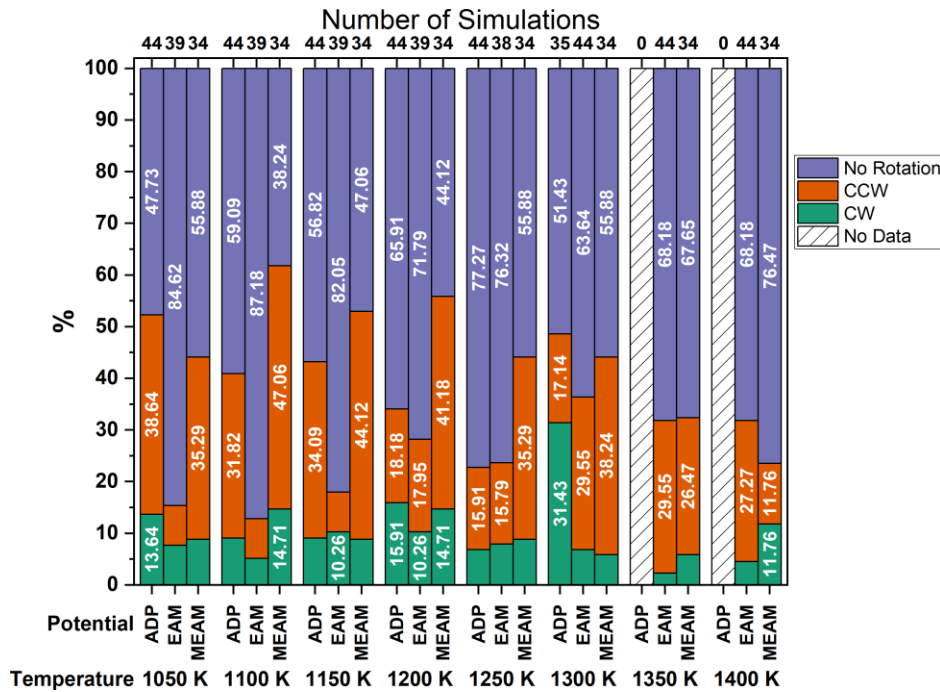


Fig. 13. Summary of the grain rotation behavior for all simulations that underwent no rotation, clockwise (CW) rotation, and counterclockwise (CCW) rotation as a function of temperature and interatomic potential. The top axis indicates the number of simulations for each potential/temperature combination. No simulations were run using the ADP potential at 1350 and 1400 K, as they were above the melting temperature predicted by the potential.

Overall, among the three potentials, the EAM potential led to the most no-rotation behavior, the ADP potential gave the most clockwise rotation, while the MEAM potential resulted in the most counterclockwise rotation. For each GB system, the grain rotational behavior is rarely consistent. In only three cases was the rotation behavior the same for every simulation for one system:  $\langle 110 \rangle$   $45^\circ$  and  $\langle 111 \rangle$   $38.2^\circ$  by the EAM potential, and  $\langle 110 \rangle$   $45^\circ$  by the MEAM potential. They all had no rotation. All other systems had mixed rotation behaviors, indicating that other factors such as temperature and stochastic effects can affect the direction of rotation.

Previous MD simulations have shown that in an FCC Cu some  $\langle 100 \rangle$  GBs tend to rotate to a specific misorientation around  $37^\circ$ .<sup>54</sup> This angle is the transition angle between the  $\langle 100 \rangle$  and  $\langle 110 \rangle$  branches of the coupling factor between the normal and tangential GB velocities. If the same rotation tendency can be applied to the BCC structure as in this study, the expected rotation behavior would be counterclockwise for the  $\langle 100 \rangle$   $20^\circ$  and  $30^\circ$  boundaries and clockwise for the  $\langle 100 \rangle$   $45^\circ$  boundary. In this work, only the  $\langle 100 \rangle$   $20^\circ$  by the MEAM potential (Fig. 12) is consistent with this expectation, though this could be just a coincidence. Therefore, the grain rotation behavior in BCC  $\gamma$  U is very different from that observed in FCC Cu.

#### 4. Discussion

In this work, different interatomic potentials resulted in different GB mobilities (values, anisotropy, temperature dependence), even if for the same GB type. This is not unique to this work, as a recent study examining the GB mobility behavior in FCC Ni using four different interatomic potentials found that the potential plays a strong role in the calculated GB mobilities.<sup>73</sup> The EAM potential used in this work was developed to model defect evolution in the U-Mo system, including the presence of Xe gaseous fission products.<sup>57</sup> Even though this potential was aimed at modeling U-Mo alloys, it captures the physical properties of pure U fairly well for the  $\gamma$  phase. However, it predicts a much higher vacancy formation energy compared to experiments.<sup>57,74</sup> Although it has been found that an interstitial mechanism dominates the self-diffusion in bulk  $\gamma$  U,<sup>74-76</sup> the vacancy formation and migration at a GB region could still play an important role on mass transport during boundary migration. The ADP potential was developed with a special focus on two metastable phases that both pure U and U-Mo systems go through when quenched.<sup>55</sup> This potential overestimates the vacancy formation energy in bulk  $\gamma$  U,<sup>74</sup> like in the EAM potential. The focus of the MEAM potential is the atomic directional bonding, with the fitting procedure focused on vacancy mobility and the energy hierarchies of different phases as calculated using first principles. Additionally, there is a stronger focus on accurately describing the  $\alpha$  U  $\rightarrow$   $\gamma$  U phase transformation at high temperatures (note that the  $\beta$  phase is ignored in this potential due to its narrow temperature range in which it exists).<sup>56</sup> To the best of the authors' knowledge, GB properties were not directly considered during the development of these potentials. Therefore, it is reasonable that these potentials have large discrepancies in predicting GB properties, including the mobility studied here.

Since GB motion is related to the atom transfer across the boundary plane, point defect diffusion could have a potential correlation with the GB mobility. At the GB region, it is likely that both interstitials and vacancies contribute to the GB motion. Previously, the defect self-diffusion coefficients in pure bulk U (which consider both interstitial and vacancy contributions) predicted by the same potentials as used in this work (except for the MEAM potential) have been reported.<sup>55,74</sup> In general, the EAM potential predicts a slower self-diffusion coefficient than the ADP potential at the same temperature. For example, at 1000 K, the EAM potential predicts<sup>74</sup>  $10^{-}$

$13 \text{ m}^2/\text{s}$  while the ADP potential predicts<sup>55</sup>  $10^{-12} \text{ m}^2/\text{s}$  for the bulk self-diffusion coefficient. If the GB mobility trend follows the bulk self-diffusion trend, the EAM potential should result in a slower GB mobility than the ADP potential. The GB mobility results from this work indicate that in general this is true especially at low temperatures, although the two potentials predict similar mobilities at high temperatures. On the other hand, for the self-diffusion at GBs, previous studies show that GB self-diffusion does not have a strong correlation with the GB mobility, and they can be considered as two distinct processes.<sup>33,77</sup> Therefore, it seems that GB mobility might not have a simple relationship with the point defect self-diffusion in the bulk or GB region. More systematic studies are certainly needed for clarifying this topic in the future.

Like in many previous studies of using curved GBs to calculate the mobility,<sup>54</sup> the cylindrical GBs created in this work may contain a high-concentration of defects, primarily vacancies due to the removal of overlapping atoms at the GB. To achieve the equilibrium defect concentration at a GB, some novel methods such as the evolutionary algorithm<sup>78</sup> and GB annealing with an open surface<sup>79,80</sup> can be used, especially for flat GBs. It has been shown in these studies that the equilibrium GB structures can be very different from the as-created ones. Unfortunately, such an approach was not employed for the curved GBs studied in this work. The high defect concentration at a GB may lead to artificially high GB mobilities. For example, Korneva et al.<sup>81</sup> compared the MD-calculated mobilities using different GB geometries (flat, spherical, and polycrystalline) and found that the spherical or curved GBs lead to a much smaller activation energy than other GB geometries. Therefore, future studies should pay more attention to the effects of oversaturated defect concentration on the mobility of curved GBs.

In FCC Al, the experimental results show that GBs with the  $\langle 111 \rangle$  rotation axis typically have faster mobilities than  $\langle 100 \rangle$  and  $\langle 110 \rangle$  rotation axes at most misorientations, although sometimes the  $\langle 100 \rangle$  rotation axis can have comparable mobilities with  $\langle 111 \rangle$  rotation axis.<sup>39</sup> If Al is representative of FCC metals in terms of mobility anisotropy, it can be argued that  $\langle 111 \rangle$  GBs are fastest in FCC metals. However, from Fig. 9,  $\langle 111 \rangle$  GBs in BCC U are never the fastest, sometimes the slowest. Therefore, it seems that the mobility anisotropy related to rotation axis for FCC metals cannot be applied to BCC metals, at least for the  $\gamma$  U studied here. In this work, the  $\langle 110 \rangle$  boundaries have the fastest mobilities in almost all cases (Fig. 9). To the best of the authors' knowledge, currently there is no reasonable explanation about why a particular rotation axis can have faster GB mobilities than other rotation axes in both FCC and BCC materials. This could be explained from the viewpoint of atomic planar density. In the cylindrical grain system (Fig. 1), the X-Y plane is perpendicular to the rotation axis (the Z direction). This plane is also perpendicular to the GB plane. To have GB motion, atoms need to diffuse across the GB plane according to Burke and Turnbull's theory.<sup>64</sup> In the Results section, the MSD analysis shows that if the atomic motion in the X-Y plane is high, then the boundary typically moves fast, although there are also some exceptions. If the X-Y plane has a high atomic planar density, then the mass transport within that plane should be more efficient than other lower-density planes due to its short in-plane interatomic distance. The highest density plane is  $\{111\}$  in FCC materials and  $\{110\}$  in BCC materials, which are consistent with the observations that the fastest GBs are  $\langle 111 \rangle$  boundaries in FCC Al and  $\langle 110 \rangle$  boundaries in BCC U. In BCC materials, the atomic planar density from high to low is:  $\rho_{110} > \rho_{100} > \rho_{111}$ . If GB mobility anisotropy is fully determined by the planar density, the mobility order in BCC materials should be  $M_{110} > M_{100} > M_{111}$ . In Fig. 9, only the EAM potential predicts this trend, and only for the  $30^\circ$  misorientation. In other cases,  $\langle 111 \rangle$  boundaries

have faster or similar mobilities compared to  $\langle 100 \rangle$  boundaries. Therefore, the planar density argument seems to only work for predicting the fastest boundaries in BCC  $\gamma$  U. This is reasonable because GB migration mechanisms are complex (e.g., atomic shuffles<sup>51,52,66</sup>) and different mechanisms may be activated at different conditions. For FCC materials, the atomic planar density order is:  $\rho_{111} > \rho_{100} > \rho_{110}$ . The experimental results of FCC Al<sup>39</sup> seem to be consistent with this order, although exceptions do exist.

Experimentally, the average GB mobilities ( $K$ ) can be extracted from grain growth experiments using the ideal grain growth equation (Eq. (1)). Here the authors use either the directly reported mobility values in literature, or an estimate of the mobilities based on the reported grain sizes at different annealing times according to Eq. (1). It should be noted that U-based alloys (e.g., U-7Mo, U-10Mo)<sup>11,23,27,30,31</sup> rather than pure U were studied in experiments. Figure 14 shows the comparison between the MD-calculated mobilities in this work and the experimentally extracted values at different temperatures. Note that the comparison of GB mobilities between MD and experiments is in the same temperature range. Clearly, the MD values are about 5 – 6 orders of magnitude higher than the experimental values. Interestingly, the slope of the lower bound of the MD-calculated mobilities is similar to the slope of the experimental data, though this is likely coincidental. The large discrepancies in GB mobility between MD simulations and experiments have been observed in other systems as well, such as UO<sub>2</sub>,<sup>33</sup> among others.<sup>82,83</sup> There could be a number of reasons for the large discrepancies. First, the material in MD simulations is pure U without any impurities or solutes (so the calculated mobilities are intrinsic for  $\gamma$  U), while the materials in experiments are U-Mo based alloys that could contain many impurities in addition to Mo solute (so the extracted mobilities are extrinsic). Although solutes and impurities can have complex effects on GB motion, in general they can cause solute drag effects and reduce the effective GB mobilities.<sup>39</sup> Second, GB migration is driven by curvature in this work. It has been argued that such a driven method may result in artificially high GB mobilities compared to the zero-driving-force method such as the random walk method.<sup>69,70,81,84</sup> However, this argument is also controversial. For example, a comparison of three methods (thermal gradient driven, curvature driven, and random walk) in a UO<sub>2</sub> system reveals that different simulation methods give similar GB mobilities.<sup>33</sup> In addition, a comparison between the stress-driven and random-walk methods also shows that they predict similar GB mobilities in Ni.<sup>85</sup> Third, as discussed earlier, the cylindrical GBs created in this work may contain oversaturated defects. Such defects may promote the GB migration and lead to artificially high GB mobilities than in experiments.

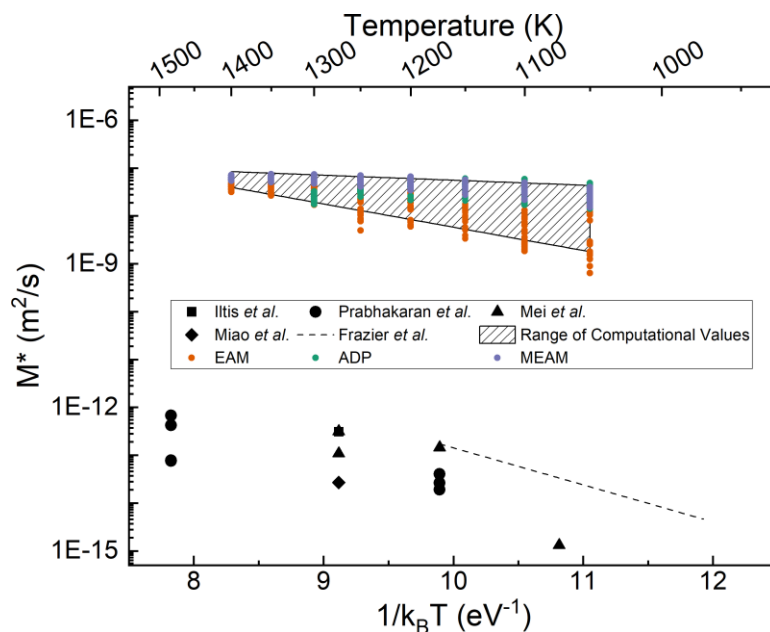


Fig. 14. Comparison of GB mobilities (in an Arrhenius plot) between the calculated values in this work and extracted values from experiments at different temperatures. The hatched region represents the upper and lower bounds of calculated values and are bounded by the mobilities of the MEAM  $\langle 110 \rangle 30^\circ$  GB (upper bound) and the EAM  $\langle 100 \rangle 45^\circ$  GB (lower bound) as calculated based on their activation energies and mobility prefactors. Experimental values are as follows: Ilitis *et al.*,<sup>31</sup> Prabhakaran *et al.*,<sup>30</sup> Mei *et al.*,<sup>23</sup> Miao *et al.*,<sup>11</sup> and Frazier *et al.*<sup>27</sup> Note that the bottom axis is  $1/(k_B T)$ , while the top axis shows the absolute temperature on a reversed scale (temperature decreases from left to right).

## 5. Conclusions

In this work, MD was used to perform many curvature-driven grain growth simulations for ten unique cylindrical GBs using three interatomic potentials (EAM, ADP, MEAM) for the pure BCC  $\gamma$  U system across a wide range of temperatures. To the best of the authors' knowledge, this is the first computational study to directly calculate the mobilities of individual GBs in this system. The obtained GB mobilities and the associated anisotropy could be used in mesoscale modeling to study grain growth in U-based metallic fuels.

In terms of GB mobility anisotropy, both misorientation and rotation axis dependencies have been investigated. Although the anisotropy does exist, the trend depends strongly on the interatomic potential. Nevertheless, the mobilities of the  $\langle 110 \rangle$  boundaries are consistently found to be the fastest for the same misorientation using three potentials. The origin of this anisotropy trend is interpreted based on the viewpoint of atomic planar density. In BCC metals, the  $\{110\}$  plane has the highest planar density. This plane is perpendicular to the GB plane and the rotation axis for the circular GBs studied in this work. The high atomic density (and therefore the short in-plane nearest-neighbor distance) may facilitate the mass transport across the GB plane and thus the GB migration. This planar density argument can also be applied to explain why in experiments the  $\langle 111 \rangle$  boundaries in FCC Al are the fastest. However, this argument cannot be applied to the

$\langle 100 \rangle$  and  $\langle 111 \rangle$  boundaries in this work's BCC U results, suggesting that additional aspects need to be considered to predict the rotation-axis-dependent GB mobility trends.

This work also finds that the interatomic potential plays a strong role in the GB mobility – in terms of both magnitude and anisotropy. This suggests that the results from MD simulations should be carefully interpreted, as some phenomena or trends could be specific for a potential. For the temperature dependence, sometimes GB mobility does not follow perfect Arrhenius behavior. Nonlinear behaviors (e.g., anti-thermal and athermal) have been observed, similar to many other studies. This observation suggests that GB migration is a complex process and that multiple migration mechanisms may operate simultaneously. The Arrhenius assumption for the temperature dependence of GB mobility may not be sufficient to describe the GB migration behavior at all temperatures.

During the cylindrical GB migration in this work, the inner grain can either have no rotation, or rotate in the clockwise/counterclockwise directions. The statistics show that in most cases the inner grain has no rotation. For the cases with rotation, the rotation direction seems stochastic because no correlation can be established with rotation axis, misorientation angle, or interatomic potential. Finally, MD-calculated GB mobilities in pure U were compared with the experimentally extracted average mobilities in U-Mo based alloys, the latter of which assumes ideal grain growth behavior. Similar to other systems such as  $\text{UO}_2$ , the calculated mobilities are about 5 – 6 orders of magnitude higher than the experimental values. The possible underlying causes for the large discrepancies are discussed in the context of solute drag effects and the large driving forces used in simulations.

## Acknowledgments

J.F. acknowledges that this material is based upon work supported under an Integrated University Program Graduate Fellowship sponsored by the U.S. Department of Energy Office of Nuclear Energy. X.M.B. acknowledges his Startup fund and the Thomas G. Digges and Thomas G. Digges Jr. Faculty Fellowship at Virginia Tech. X.M.B. also acknowledges the Faculty Joint Appointment Program at Idaho National Laboratory. The authors acknowledge the use of the computing facilities at the Advanced Research Computing (ARC) at Virginia Tech. This manuscript has been co-authored by Battelle Energy Alliance, LLC under Contract No. DE-AC07-05ID14517 with the U.S. Department of Energy. The United States Government retains and the publisher, by accepting the article for publication, acknowledges that the United States Government retains a nonexclusive, paid-up, irrevocable, world-wide license to publish or reproduce the published form of this manuscript, or allow others to do so, for United States Government purposes.

## References

1. Senior, D. J. & Burkes, D. E. *Fuel Fabrication Capability Research and Development Plan*. <https://www.osti.gov/biblio/1149235> (2014) doi:10.2172/1149235.
2. Wilson, E. H., Jaluvka, D., Hebden, A. S., Stillman, J. A. & Jamison, L. M. U.S. High Performance Research Reactor Preliminary Design Milestone for Conversion to Low Enriched Uranium Fuel. in (2019).
3. Pugh, S. F. Swelling in alpha uranium due to irradiation. *Journal of Nuclear Materials* **4**, 177–199 (1961).
4. Di Lemma, F. G. *et al.* Investigation of the microstructure evolution of alpha uranium after in pile transient. *Journal of Nuclear Materials* **542**, 152467 (2020).
5. Meyer, M. K. *et al.* Irradiation Performance of U-Mo Monolithic Fuel. *Nuclear Engineering and Technology* **46**, 169–182 (2014).
6. Donohue, J. & Einspahr, H. The Structure of  $\beta$ -Uranium. *Acta Crystallographica Section B: Structural Crystallography and Crystal Chemistry* **27**, 1740–1743 (1971).
7. Nuclear Research Reactors - World Nuclear Association. <https://world-nuclear.org/information-library/non-power-nuclear-applications/radioisotopes-research/research-reactors.aspx>.
8. Ajantiwalay, T., Smith, C., Keiser, D. D. & Aitkaliyeva, A. A critical review of the microstructure of U–Mo fuels. *Journal of Nuclear Materials* **540**, 152386 (2020).
9. Sinha, V. P., Hegde, P. V., Prasad, G. J., Dey, G. K. & Kamath, H. S. Phase transformation of metastable cubic  $\gamma$ -phase in U–Mo alloys. *Journal of Alloys and Compounds* **506**, 253–262 (2010).
10. Rest, J., Kim, Y. S., Hofman, G. L., Meyer, M. K. & Hayes, S. L. *U-Mo fuels handbook. Version 1.0*. <https://www.osti.gov/biblio/1335129> (2006) doi:10.2172/1335129.
11. Miao, Y. *et al.* An exploration of measuring lower-length-scale structures in nuclear materials: Thermal conductivity of U-Mo fuel particle. *Journal of Nuclear Materials* **527**, 151797 (2019).
12. Hengstler, R. M. *et al.* Physical properties of monolithic U8wt.%–Mo. *Journal of Nuclear Materials* **402**, 74–80 (2010).

13. Van den Berghe, S., Van Renterghem, W. & Leenaers, A. Transmission electron microscopy investigation of irradiated U–7wt%Mo dispersion fuel. *Journal of Nuclear Materials* **375**, 340–346 (2008).
14. Meyer, M. K. *et al.* Low-temperature irradiation behavior of uranium–molybdenum alloy dispersion fuel. *Journal of Nuclear Materials* **304**, 221–236 (2002).
15. Kim, Y. S., Hofman, G. L. & Cheon, J. S. Recrystallization and fission-gas-bubble swelling of U–Mo fuel. *Journal of Nuclear Materials* **436**, 14–22 (2013).
16. Van den Berghe, S. *et al.* Swelling of U(Mo) dispersion fuel under irradiation – Non-destructive analyses of the SELENIUM plates. *Journal of Nuclear Materials* **442**, 60–68 (2013).
17. Rest, J. A model for the effect of the progression of irradiation-induced recrystallization from initiation to completion on swelling of UO<sub>2</sub> and U–10Mo nuclear fuels. *Journal of Nuclear Materials* **346**, 226–232 (2005).
18. Robinson, A. B. *et al.* Swelling of U-Mo Monolithic Fuel: Developing a Predictive Swelling Correlation under Research Reactor Conditions. *Journal of Nuclear Materials* **544**, 152703 (2021).
19. Gan, J. *et al.* Microstructural characterization of irradiated U–7Mo/Al–5Si dispersion fuel to high fission density. *Journal of Nuclear Materials* **454**, 434–445 (2014).
20. Leenaers, A., Van Renterghem, W. & Van den Berghe, S. High burn-up structure of U(Mo) dispersion fuel. *Journal of Nuclear Materials* **476**, 218–230 (2016).
21. Noirot, J., Desgranges, L. & Lamontagne, J. Detailed characterisations of high burn-up structures in oxide fuels. *Journal of Nuclear Materials* **372**, 318–339 (2008).
22. Liang, L. *et al.* Mesoscale model for fission-induced recrystallization in U-7Mo alloy. *Computational Materials Science* **124**, 228–237 (2016).
23. Mei, Z.-G. *et al.* Grain growth in U–7Mo alloy: A combined first-principles and phase field study. *Journal of Nuclear Materials* **473**, 300–308 (2016).
24. Liang, L., Mei, Z.-G. & Yacout, A. M. Fission-induced recrystallization effect on intergranular bubble-driven swelling in U-Mo fuel. *Computational Materials Science* **138**, 16–26 (2017).

25. Hu, S., Burkes, D., Lavender, C. A. & Joshi, V. Effect of grain morphology on gas bubble swelling in UMo fuels – A 3D microstructure dependent Booth model. *Journal of Nuclear Materials* **480**, 323–331 (2016).
26. Hu, S., Joshi, V. & Lavender, C. A. A Rate-Theory–Phase-Field Model of Irradiation-Induced Recrystallization in UMo Nuclear Fuels. *JOM* **69**, 2554–2562 (2017).
27. Frazier, W. E., Hu, S., Overman, N., Lavender, C. & Joshi, V. V. Short communication on Kinetics of grain growth and particle pinning in U-10 wt.% Mo. *Journal of Nuclear Materials* **498**, 254–258 (2018).
28. Tonks, M. R., Gaston, D., Millett, P. C., Andrs, D. & Talbot, P. An object-oriented finite element framework for multiphysics phase field simulations. *Computational Materials Science* **51**, 20–29 (2012).
29. Clarke, A. J. *et al.* Microstructural evolution of a uranium-10 wt.% molybdenum alloy for nuclear reactor fuels. *Journal of Nuclear Materials* **465**, 784–792 (2015).
30. Prabhakaran, R., Gardner, L., Joshi, V., Burkes, D. & Lavender, C. Effect of homogenization and hot rolling on the mechanical properties, microstructure and corrosion behavior of U–10Mo monolithic fuel. *Journal of Nuclear Materials* **527**, 151804 (2019).
31. Iltis, X. *et al.* Microstructure of as atomized and annealed U-Mo<sub>7</sub> particles: A SEM/EBSD study of grain growth. *Journal of Nuclear Materials* **495**, 249–266 (2017).
32. Thompson, C. V. Grain Growth in Thin Films. *Annu. Rev. Mater. Sci.* **20**, 245 (1990).
33. Bai, X.-M., Zhang, Y. & Tonks, M. R. Testing thermal gradient driving force for grain boundary migration using molecular dynamics simulations. *Acta Materialia* **85**, 95–106 (2015).
34. Frazier, W. E., Hu, S., Overman, N., Lavender, C. & Joshi, V. V. Simulations of post-recrystallization grain growth in monolithic U–10Mo fuel processing. *Journal of Nuclear Materials* **526**, 151763 (2019).
35. Chen, K., Han, J., Pan, X. & Srolovitz, D. J. The grain boundary mobility tensor. *Proc Natl Acad Sci USA* **117**, 4533–4538 (2020).
36. Read, W. T. & Shockley, W. Dislocation Models of Crystal Grain Boundaries. *Phys. Rev.* **78**, 275–289 (1950).
37. Beeler, B., Zhang, Y. & Gao, Y. An atomistic study of grain boundaries and surfaces in  $\gamma$ U-Mo. *Journal of Nuclear Materials* **507**, 248–257 (2018).

38. Molodov, D. A., Czubayko, U., Gottstein, G. & Shvindlerman, L. S. On the effect of purity and orientation on grain boundary motion. *Acta Materialia* **46**, 553–564 (1998).
39. Gottstein, G. & Shvindlerman, L. S. *Grain Boundary Migration in Metals: Thermodynamics, Kinetics, Applications*. (CRC Press, 2010).
40. Upmanyu, M. *et al.* Boundary Mobility and Energy Anisotropy Effects on Microstructural Evolution During Grain Growth. *Interface Science* **10**, 201–216 (2002).
41. Kazaryan, A., Wang, Y., Dregia, S. A. & Patton, B. R. Grain growth in systems with anisotropic boundary mobility: Analytical model and computer simulation. *Phys. Rev. B* **63**, 184102 (2001).
42. Kazaryan, A., Wang, Y., Dregia, S. A. & Patton, B. R. Grain growth in anisotropic systems: comparison of effects of energy and mobility. *Acta Materialia* **50**, 2491–2502 (2002).
43. Tonks, M. R., Simon, P.-C. A. & Hirschhorn, J. Mechanistic grain growth model for fresh and irradiated UO<sub>2</sub> nuclear fuel. *Journal of Nuclear Materials* **543**, 152576 (2021).
44. Novikov, V. Yu. Crystallographic texture and grain growth. *Materials Letters* **254**, 230–232 (2019).
45. Ma, N., Kazaryan, A., Dregia, S. A. & Wang, Y. Computer simulation of texture evolution during grain growth: effect of boundary properties and initial microstructure. *Acta Materialia* **52**, 3869–3879 (2004).
46. Rohrer, G. S. *et al.* Comparing calculated and measured grain boundary energies in nickel. *Acta Materialia* **58**, 5063–5069 (2010).
47. Olmsted, D. L., Foiles, S. M. & Holm, E. A. Survey of computed grain boundary properties in face-centered cubic metals: I. Grain boundary energy. *Acta Materialia* **57**, 3694–3703 (2009).
48. Olmsted, D. L., Holm, E. A. & Foiles, S. M. Survey of computed grain boundary properties in face-centered cubic metals—II: Grain boundary mobility. *Acta Materialia* **57**, 3704–3713 (2009).
49. Rollett, A. D., Gottstein, G., Shvindlerman, L. S. & Molodov, D. A. Grain boundary mobility – a brief review. *MEKU* **95**, 226–229 (2004).
50. Taheri, M. L., Molodov, D. A., Gottstein, G. & Rollett, A. D. Grain boundary mobility under a stored-energy driving force: a comparison to curvature-driven boundary migration. *Zeitschrift Fur Metallkunde* **96**, 1166 (2005).

51. Toda-Caraballo, I., Bristowe, P. D. & Capdevila, C. A molecular dynamics study of grain boundary free energies, migration mechanisms and mobilities in a bcc Fe–20Cr alloy. *Acta Materialia* **60**, 1116–1128 (2012).
52. Zhou, L., Zhou, N. & Song, G. Collective motion of atoms in grain boundary migration of a bcc metal. *Philosophical Magazine* **86**, 5885–5895 (2006).
53. Zhang, H., Du, D., Srolovitz, D. J. & Mendeleev, M. I. Determination of grain boundary stiffness from molecular dynamics simulation. *Appl. Phys. Lett.* **88**, 121927 (2006).
54. Trautt, Z. T. & Mishin, Y. Grain boundary migration and grain rotation studied by molecular dynamics. *Acta Materialia* **60**, 2407–2424 (2012).
55. Starikov, S. V., Kolotova, L. N., Kuksin, A. Yu., Smirnova, D. E. & Tseplyaev, V. I. Atomistic simulation of cubic and tetragonal phases of U-Mo alloy: Structure and thermodynamic properties. *Journal of Nuclear Materials* **499**, 451–463 (2018).
56. Fernández, J. R. & Pascuet, M. I. On the accurate description of uranium metallic phases: a MEAM interatomic potential approach. *Modelling and Simulation in Materials Science and Engineering* **22**, 055019 (2014).
57. Smirnova, D. E. *et al.* A ternary EAM interatomic potential for U–Mo alloys with xenon. *Modelling and Simulation in Materials Science and Engineering* **21**, 035011 (2013).
58. Plimpton, S. Fast Parallel Algorithms for Short-Range Molecular Dynamics. *Journal of Computational Physics* **117**, 1–19 (1995).
59. Wilson, A. S. & Rundle, R. E. The structures of uranium metal. *Acta Crystallographica* **2**, 126–127 (1949).
60. Grenthe, I. *et al.* Uranium. in *The Chemistry of the Actinide and Transactinide Elements* (eds. Morss, L. R., Edelstein, N. M. & Fuger, J.) 253–698 (Springer Netherlands, 2006). doi:10.1007/1-4020-3598-5\_5.
61. Ulomek, F., O’Brien, C. J., Foiles, S. M. & Mohles, V. Energy conserving orientational force for determining grain boundary mobility. *Modelling and Simulation in Materials Science and Engineering* **23**, 025007 (2015).
62. Jekel, C. F. & Venter, G. *pwlf: A Python Library for Fitting 1D Continuous Piecewise Linear Functions.* (2019).
63. Cantwell, P. R., Holm, E. A., Harmer, M. P. & Hoffmann, M. J. Anti-thermal behavior of materials. *Scripta Materialia* **103**, 1–5 (2015).

64. Burke, J. E. & Turnbull, D. Recrystallization and grain growth. *Progress in Metal Physics* **3**, 220–292 (1952).
65. Fensin, S. J. *et al.* Structural disjoining potential for grain-boundary premelting and grain coalescence from molecular-dynamics simulations. *Phys. Rev. E* **81**, 031601 (2010).
66. O’Brien, C. J. & Foiles, S. M. Exploration of the mechanisms of temperature-dependent grain boundary mobility: search for the common origin of ultrafast grain boundary motion. *Journal of Materials Science* **51**, 6607–6623 (2016).
67. Ulomek, F. & Mohles, V. Separating grain boundary migration mechanisms in molecular dynamics simulations. *Acta Materialia* **103**, 424–432 (2016).
68. Zhang, H., Srolovitz, D. J., Douglas, J. F. & Warren, J. A. Grain boundaries exhibit the dynamics of glass-forming liquids. *Proceedings of the National Academy of Sciences* **106**, 7735–7740 (2009).
69. Deng, C. & Schuh, C. A. Atomistic Simulation of Slow Grain Boundary Motion. *Phys. Rev. Lett.* **106**, 045503 (2011).
70. Deng, C. & Schuh, C. A. Diffusive-to-ballistic transition in grain boundary motion studied by atomistic simulations. *Phys. Rev. B* **84**, 214102 (2011).
71. Rheinheimer, W., Schoof, E., Selzer, M., Nestler, B. & Hoffmann, M. J. Non-Arrhenius grain growth in strontium titanate: Quantification of bimodal grain growth. *Acta Materialia* **174**, 105–115 (2019).
72. Homer, E. R., Holm, E. A., Foiles, S. M. & Olmsted, D. L. Trends in Grain Boundary Mobility: Survey of Motion Mechanisms. *JOM* **66**, 114–120 (2014).
73. Chesser, I. & Holm, E. Understanding the anomalous thermal behavior of  $\Sigma 3$  grain boundaries in a variety of FCC metals. *Scripta Materialia* **157**, 19–23 (2018).
74. Smirnova, D. E., Kuksin, A. Yu., Starikov, S. V. & Stegailov, V. V. Atomistic modeling of the self-diffusion in  $\gamma$ -U and  $\gamma$ -U-Mo. *Phys. Metals Metallogr.* **116**, 445–455 (2015).
75. Smirnova, D. E., Kuksin, A. Yu. & Starikov, S. V. Investigation of point defects diffusion in bcc uranium and U–Mo alloys. *Journal of Nuclear Materials* **458**, 304–311 (2015).
76. Park, G., Beeler, B. & Okuniewski, M. A. An atomistic study of defect energetics and diffusion with respect to composition and temperature in  $\gamma$ U and  $\gamma$ U-Mo alloys. *Journal of Nuclear Materials* **552**, 152970 (2021).

77. Schönfelder, B., Gottstein, G. & Shvindlerman, L. S. Comparative study of grain-boundary migration and grain-boundary self-diffusion of [001] twist-grain boundaries in copper by atomistic simulations. *Acta Materialia* **53**, 1597–1609 (2005).
78. Frolov, T. *et al.* Grain boundary phases in bcc metals. *Nanoscale* **10**, 8253–8268 (2018).
79. Starikov, S., Mrovec, M. & Drautz, R. Study of grain boundary self-diffusion in iron with different atomistic models. *Acta Materialia* **188**, 560–569 (2020).
80. Frolov, T. & Mishin, Y. Molecular dynamics modeling of self-diffusion along a triple junction. *Phys. Rev. B* **79**, 174110 (2009).
81. Korneva, M. A., Starikov, S. V., Zhilyaev, A. P., Akhatov, I. S. & Zhilyaev, P. A. Atomistic Modeling of Grain Boundary Migration in Nickel. *Adv. Eng. Mater.* **22**, 2000115 (2020).
82. Janssens, K. G. F. *et al.* Computing the mobility of grain boundaries. *Nature Materials* **5**, 124–127 (2006).
83. Zhang, H., Upmanyu, M. & Srolovitz, D. J. Curvature driven grain boundary migration in aluminum: molecular dynamics simulations. *Acta Materialia* **53**, 79–86 (2005).
84. Trautt, Z. T., Upmanyu, M. & Karma, A. Interface Mobility from Interface Random Walk. *Science* **314**, 632 (2006).
85. Mendeleev, M. I., Deng, C., Schuh, C. A. & Srolovitz, D. J. Comparison of molecular dynamics simulation methods for the study of grain boundary migration. *Modelling and Simulation in Materials Science and Engineering* **21**, 045017 (2013).